JOURNAL OF GEOPHYSICAL RESEARCH, VOL. 116, D14117, doi:10.1029/2011JD015654, 2011

# Space-time cascades and the scaling of ECMWF reanalyses: Fluxes and fields

S. Lovejoy[1] and D. Schertzer[2,3]

Received 19 January 2011; revised 20 April 2011; accepted 27 April 2011; published 29 July 2011.

[1] We consider the space-time scaling properties of the European Centre for Medium-Range Weather Forecasts (ECMWF) interim reanalysis products for the wind ($u$, $v$, $w$), humidity ($h_s$), temperature ($T$), and geopotentials ($z$) and their corresponding turbulent fluxes using the daily 700 mbar products for the year 2006. Following previous studies on $T$, $h_s$, and $u$, we show that that the basic predictions of multiplicative cascade models are well respected over space-time scales below ~5000 km, shorter than ~5–10 days providing precise scale by scale determination of the reanalysis statistical properties (needed for example for stochastic parameterizations in ensemble forecasting systems). We innovate by including the meridional and vertical wind components ($v$, $w$) and geopotential ($z$), and by considering their horizontal anisotropies, their latitudinal variations and, perhaps most importantly, by directly analyzing the fields (not just fluxes). Whereas the fluxes have nearly isotropic exponents in space-time with little latitudinal variation (displaying only scale independent "trivial" anisotropy), the fields have significant scaling horizontal anisotropies. These complicate the interpretation of standard isotropic spectra and are likely to be artifacts. Many of the new (nonconservation) exponents ($H$) are nonstandard and currently have no adequate theoretical explanation although the key horizontal wind and temperature $H$ exponents may be consequences of horizontal Kolmogorov scaling, combined with sloping isobaric surfaces. In time the scaling is broken at around 5–10 days, i.e., roughly the lifetime of planetary structures; lower frequencies are spectrally flatter: the "spectral plateau," weather-low-frequency weather regime.

**Citation:** Lovejoy, S., and D. Schertzer (2011), Space-time cascades and the scaling of ECMWF reanalyses: Fluxes and fields, *J. Geophys. Res.*, *116*, D14117, doi:10.1029/2011JD015654.

## 1. Introduction: Analyses, Reanalyses, Fluxes, and Fields

[2] The advent of high quality global scale data sets has finally made it possible to systematically study the space-time statistical properties of the atmosphere as a function of scale. Yet, all empirical analyses suffer from limitations. For example, data from global scale networks are invariably sparse [*Lovejoy et al.*, 1986] and aircraft data are not only limited to 1-D transects, but have nontrivial problems of interpretation due to trajectories which are both fractal and sloping [*Lovejoy et al.*, 2004, 2009c]. Although satellite data are nearly ideal in terms of their coverage from global scales down to kilometric (or less), they measure radiances rather than variables of state and their scale by scale statistical properties have received little attention.

[3] The alternative source of global scale data studied in this paper is the reanalyses. These are hybrid products obtained by using much of the available data from both in situ networks and satellites but which are processed with the help of complex data assimilation algorithms adapted for specific meteorological models. These algorithms use covariance matrices to interpolate the data onto uniform grids. The 4D VAR assimilation scheme relevant here implies that the European Centre for Medium-Range Weather Forecasts (ECMWF) interim products are solutions to the primitive equations but at the relatively low resolution of the grid: there are implicit smoothness and regularity assumptions. Hydrostaticity may also be an issue since the use of (gently sloping) isobars rather than isoheights can potentially lead to scale breaks and the spurious appearance of vertical exponents (see the discussion of isobaric aircraft statistics below). Nevertheless, at least in some cases, such as the hard to measure vertical winds, they provide the only global scale estimates; in any case they complement the "pure" instrumental data sets.

[4] A series of papers involving lidar, drop sonde, aircraft, and satellite data [see *Lovejoy and Schertzer*, 2010, 2011a,

---

[1] Department of Physics, McGill University, Montreal, Quebec, Canada.
[2] Laboratoire Eau Environnement Systèmes Urbains, Ecole des Ponts ParisTech, Université Paris Est, Marne-la-Vallée, France.
[3] Météo France, Paris, France.

0148-0227/11/2011JD015654

and references therein] presents a large body of empirical evidence that the atmosphere is accurately scale invariant from planetary scales continuing down through the mesoscale, continuing possibly to the dissipation scale. As argued by *Schertzer and Lovejoy* [1984, 1985a], such a wide scaling range is only possible if one considers generalized (anisotropic) notions of scaling; here it is sufficient to consider different scalings in different (e.g., orthogonal) directions. This means that while fluctuations $\Delta f$ in a turbulent quantity $f$ (e.g., a component of the wind) are scaling in the horizontal (lag $\Delta x$) with exponent $H_h$, i.e., $\Delta f \approx \varphi_h \Delta x^{H_h}$, then fluctuations in the vertical (lags $\Delta z$) are scaling with $\Delta f \approx \varphi_v \Delta z^{H_v}$; $\varphi_h$ and $\varphi_h$ are physically different turbulent fluxes. Note that these are fluxes through spherical shells in Fourier space, not fluxes in physical space; this is different from the classical interpretation of the quantities in terms of dissipation; the fluxes are only equal to the dissipation at the small dissipation scales. Study of the fluxes averaged/degraded in resolution show [*Lovejoy et al.*, 2009a; *Lovejoy and Schertzer*, 2010] that up until 5,000–10,000 km their statistics are nearly exactly as predicted by multiplicative cascade models (section 2, equation (1)) and that their exponent functions are nearly the same in the zonal and meridional directions. A model for the velocity field which turns out to be close to the observations takes $\varphi_h = \varepsilon^{1/3}$, $\phi_v = \phi^{1/5}$, $H_h = 1/3$ and $H_v = 3/5$, where $\varepsilon$ is the energy and $\phi$ is the buoyancy variance flux which thus dominate the dynamics, respectively, along the horizontal and vertical directions [*Schertzer and Lovejoy*, 1985b] (these correspond to the classical Kolmogorov [*Kolmogorov*, 1941] and Bolgiano-Obukhov [*Bolgiano*, 1959; *Obukhov*, 1959] exponents, but in a nonclassical anisotropic framework). As a consequence, $H_v > H_h$ for the velocity field and it seems to be a rather general property that corresponds to the fact that structures (defined as $f$ isolines) become progressively flatter and flatter at larger and larger scales, yet this stratification occurs without any characteristic size being introduced.

[5] While this horizontal/vertical anisotropy is fundamental in understanding the existence of the wide range horizontal scaling, we do not consider this vertical stratification here. Surprisingly however, it turns out that scaling anisotropy seems to be essential in understanding the horizontal (or more accurately, the isobaric) statistics of the reanalysis fields, although apparently not of the fluxes: i.e., we find $H_{EW}/H_{NS} = H_y \approx 0.80$ for all fields (with a predicted inversion for the meridional wind; "NS" and "EW" mean "north-south" and "east-west," respectively) whereas $\varphi_{NS}$ and $\varphi_{EW}$ not only have very nearly the same statistics (horizontal isotropy), but also these are very nearly those theoretically predicted for multiplicative cascade processes. While the latter result confirms those made on other reanalyses and products [*Stolle et al.*, 2009], the former is new and helps shed light on the problems encountered by the classical approaches to statistically characterizing reanalyses.

[6] To see this, recall that while the classical approaches [*Boer and Shepherd*, 1983; *Strauss and Ditlevsen*, 1999] suppose a priori the physical nature of the relevant fluxes (e.g., energy, enstrophy flux), our method has the advantage of objectively defining the fluxes using the observed fluctuations. (A disadvantage of such objectively defined fluxes is that the physical meaning of the flux is not obvious: it is a subject of future research.) However, as we review in the next section, it turns out that up until now, understanding the statistical properties of the fields $f$ (such as their spectra) has not given any clear result. We argue that that the reason is that the reanalyses are anisotropic in the horizontal with different exponents, i.e., $H_{EW} \neq H_{NS}$ (the zonal and meridional directions, respectively) and up until now only isotropic reanalysis spectra (i.e., integrated over all angles) have been considered. Whether, as we suspect, this scaling anisotropy is a spurious artifact of the reanalyses; its discovery will help settle long-standing debates about the statistical nature of the atmosphere (i.e., the classical 2D versus 3D isotropic turbulence model versus the scaling 23/9 D alternative [*Schertzer and Lovejoy*, 1985b]; see *Lovejoy and Schertzer* [2010] for a review).

[7] A final important issue we cover is the nature of the temporal variability and the relation between the spatial and temporal statistics. Since structures in the atmosphere have "lifetimes" which depend on their spatial scales; the two being connected (at least dimensionally) via a velocity, we expect that the spatial scaling of the wind will impose a regime of temporal scaling, at least up to scales corresponding the to the size of the planet; i.e., roughly 5–10 days. Indeed, virtually all meteorological fields have a drastic change in behavior at about this scale; the transition itself has been termed a "dimensional transition" [*Lovejoy and Schertzer*, 2010] and the lower frequency regime where the spectrum is significantly flatter has been called a "spectral plateau" [*Lovejoy and Schertzer*, 1986]. While the fluctuations for high frequencies are dominated by single structures and corresponding lifetimes, the fluctuations for the lower plateau frequencies are consequences of many lifetimes and have much lower statistical interdependences (lower $H$'s, lower spectral exponents) and these are accurately modeled by assuming that the space-time scaling weather cascade model continues to much lower frequencies [*Lovejoy and Schertzer*, 2010]. Interestingly, *Lovejoy and Schertzer* [2011b, 2011c] have given evidence for analogous behavior in the oceans, although with a critical time scale of ~1 year, so that due to ocean-atmosphere interactions, the behavior in the range of scales ≈ 10 days–1 year is a bit more complex.

[8] This paper is organized as follows. In section 2 we review the basic theory and data analysis techniques. In section 3, we perform systematic cascade analyses on the turbulent fluxes in the two horizontal directions and in time, we examine the statistical relation between space and time ("Stommel" diagrams), their latitudinal dependence, and the "Levy collapse" which is a test of the underlying probability distributions of the fluxes irrespective of the scaling. In section 4 we consider the fields (the observables) taking care to consider their anisotropies. We outline the necessary elements of generalized scale invariance and estimate zonal, meridional and isotropic spectral exponents; we then consider the temporal spectra and the latitudinal dependence of all the exponents. In section 5, we conclude. In Appendix A, we discuss possible biases in our anisotropy analyses due to the use of cylindrical map projections.

## 2. The Data, Fluxes, and Predictions of Multiplicative Cascades

### 2.1. The Scaling Properties of Reanalyses

[9] Study of the scaling properties of atmospheric models and reanalyses is still in its infancy. The early pioneering

**Table 1.** Space-Time Cascade Parameter Estimates[a]

| | $h_s$ | $T$ | $u$ | $v$ | $w$ | $z$ |
|---|---|---|---|---|---|---|
| $\beta$ | 1.90 | 2.40 | 2.40 | 2.40 | 0.40 | 3.35 |
| $C_{1,\mathrm{uni}}$ | 0.102 ± 0.009 | 0.077 ± 0.005 | 0.084 ± 0.006 | 0.087 ± 0.012 | 0.121 ± 0.007 | 0.088 ± 0.006 |
| $C_1$ | 0.101 ± 0.009 | 0.072 ± 0.005 | 0.082 ± 0.007 | 0.085 ± 0.013 | 0.115 ± 0.008 | 0.083 ± 0.005 |
| $\alpha$ | 1.77 ± 0.06 | 1.90 ± 0.006 | 1.85 ± 0.012 | 1.85 ± 0.011 | 1.92 ± 0.009 | 1.90 ± 0.012 |
| $H$ | 0.54 | 0.77 | 0.77 | 0.78 | −0.14 | 1.26 |
| $L_{effEW}$ (km) | 13000 | 20000 | 13000 | 16000 | 16000 | 63000 |
| $L_{effNS}$ (km) | 6300 | 16000 | 8000 | 10000 | 13000 | 40000 |
| $\tau_{eff}$ (days) | 46 | 58 | 29 | 29 | 37 | 290 |
| $V_{eff}$ (km/d) | 280 | 340 | 450 | 550 | 430 | 220 |
| $\delta$ (%) | 0.32 ± 0.04 | 0.35 ± 0.02 | 0.31 ± 0.09 | 0.28 ± 0.10 | 0.33 ± 0.10 | 0.52 ± 0.30 |

[a] Fits for $C_1$, $\alpha$ are for scales <5000 km, and the spreads in the parameters are over east-west and north-south directions and time. The temporal fits are from 2 to 8 days. The $\beta$ and hence $H$ parameter of the $v$ (meridional wind) field is only fit up to 1300 km. The spreads are standard deviations over the east-west, north-south, and temporal estimates. The $H$ estimates are for the spatial analyses only; they are from $\beta$ and $K(2)$: $H = (\beta + 1 - K(2))/2$ with $K(2)$ from the universal multifractal fits and using the $\beta$ from the isotropic, zonal, and meridional horizontal spectral analysis in section 3; they are for the east-west $H$ values (the only exception is the meridional wind where it is the north-south value); the value in the orthogonal direction can be obtained by dividing by $H_y \approx 0.80$. See Table 4 for temporal $H$ estimates.

studies of *Boer and Shepherd* [1983] and *Strauss and Ditlevsen* [1999] attempted to test the framework of two-dimensional geostrophic turbulence which at the time was believed to provide a good model for the synoptic scale dynamics. Rather than directly studying the scaling properties of the fields themselves, these authors started by converting them by vertical integration into theoretically preordained 2-D products; even these were not studied directly but rather via anomalies with respect to low-frequency means ("stationary" and "transient" parts), followed by a further decomposition into rotational and irrotational wind components. In contrast, the more recent studies have directly focused on the scaling properties of the turbulent fluxes that are expected to be the products of multiplicative cascade processes and they attempted to achieve a wide survey of reanalysis fields, intercomparing many different models, studying the variations in the cascade properties as functions of altitude, of latitude and forecast horizon [*Stolle et al.*, 2009, also The temporal cascade structure and space-time relations for reanalyses and global circulation models, submitted to *Quarterly Journal of the Royal Meteorological Society*, 2011]. The necessary compromises restricted them to temperature ($T$), the zonal wind ($u$), humidity ($h$) fields. It was found that whereas the direct analyses inspired by the scale invariance of the equations and boundary conditions generally displayed excellent scaling (especially for the turbulent fluxes), in comparison the more complex analyses inspired by quasi geostrophic theory had relatively poor scaling and their behavior was not clear (compare the results here with those of *Strauss and Ditlevsen* [1999]).

[10] If atmospheric models and reanalyses are to be realistic, they must, like the data, also have multiplicative cascade structures. This was indeed demonstrated for $T$, $h$, $u$ in (hydrostatic) weather forecast models (NOAA's GFS model and the Canadian GEM model) and on ERA40 reanalyses by *Stolle et al.* [2009] (space) and Stolle et al. (submitted manuscript, 2011) (time). Isolated results on the ECMWF interim reanalyses and the 20th century reanalysis [*Compo et al.*, 2011] have also been published [*Lovejoy and Schertzer*, 2010]; the latter in particular permit the study of long-time (>1 century) statistical behaviors. Finally, a detailed comparison [*Gires et al.*, 2011] of the rain field simulated by the (nonhydrostatic) mesoscale model MESO-NH9 with the corresponding radar rainfall radar showed that both have similar space-time scaling ranges, but with different exponents. Analogous scaling analyses have not yet been carried out for climate models (although see the review by *Lucarini and Ragone* [2011]).

[11] Qualitatively, the horizontal and temporal cascade structures of the data, models and reanalyses were found to be very similar, at least for the fluxes from the most intensely scrutinized $T$, $u$, $h$, fields. Indeed, the different fields and models share many quantitative features; this includes the outer cascade scales (in time and space) and the values (see Table 1) of the universal multifractal parameters [*Schertzer and Lovejoy*, 1987] (the mean sparseness or intermittency $C_1$, the index of multifractality $\alpha$, the nonconservation exponent $H$; these are defined below). However, there are also important differences, especially in the vertical direction presumably associated with the hydrostatic approximation used in most of the cited models and reanalyses. In addition, the scaling of the model/reanalysis fields (as opposed to the underlying turbulent fluxes) was not systematically studied at all but clearly suffered from important differences with the data, especially the horizontal velocity field which *Lovejoy et al.* [2010] had already found displayed the vertical rather than horizontal scaling exponent. This fact was attributed to the isobaric nature of the available reanalysis levels (the small but nonzero isobaric slopes are expected to lead to the same spurious scaling as in the aircraft data and for the same reasons [*Lovejoy et al.*, 2009c]).

[12] So far, statistical studies of reanalyses have provided only a partial view of this vast "landscape" of models and products; below we extend these in three important ways: first, to study the statistics of the fields themselves (rather than just their turbulent fluxes) in particular to estimate the spectral exponents; second, to extend the analyses to other fields—the meridional and vertical winds ($v$, $w$)—and to the geopotential height ($z$); third, to address the issue of north-south versus east-west anisotropy, which turns out to be linked to the first. We do this using the state-of-the-art ECMWF interim reanalysis, chosen because of its high resolution, its ready availability and the fact that its overall quality is recognized as high by the meteorological com-

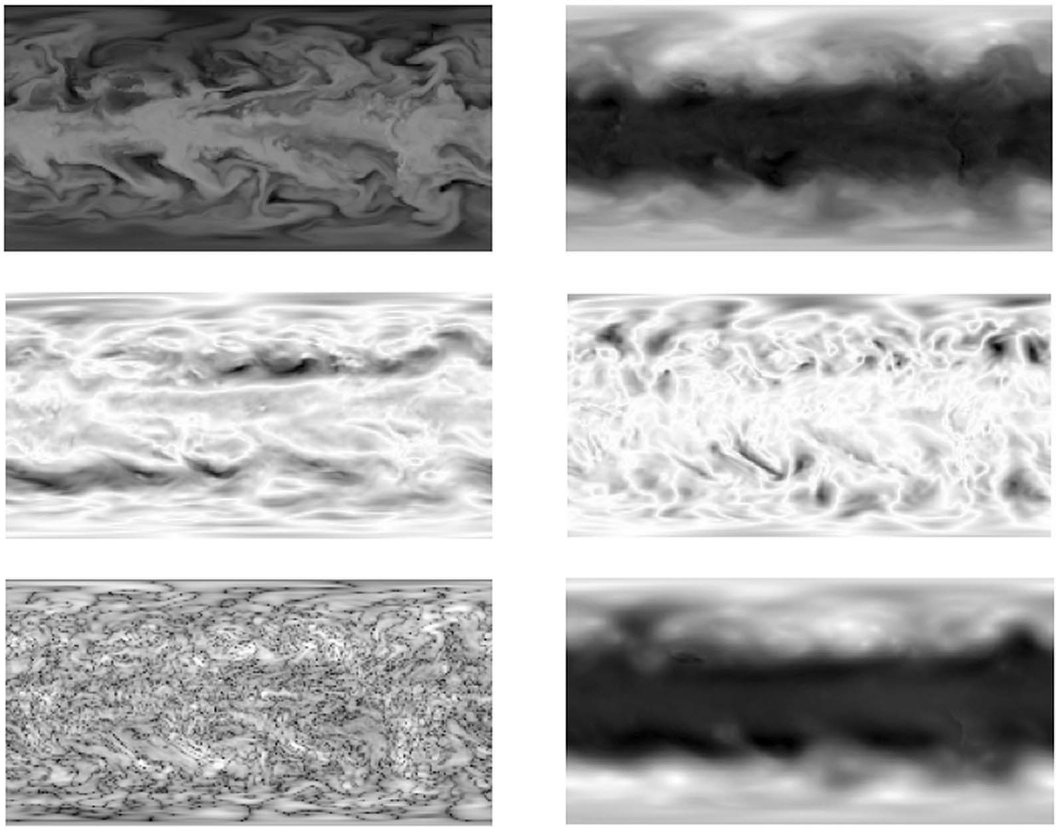

**Figure 1.** Grey shade renderings of the ECMWF interim reanalyses for 0000 UT, 1 January 2006, on the 700 mbar pressure surface (top left) Specific humidity, (top right) temperature, (middle left) zonal wind, (middle right) meridional wind, (bottom left) vertical wind (in pressure coordinates), and (bottom right) the geopotential field.

munity. We specifically focused on the 700 mbar level as being representative of the "free" atmosphere (without too many issues caused by the topography) and we studied the daily (0000 UT products) for the entire year 2006 primarily focusing on a band between ±45° latitude, but with some systematic surveys of latitudinal variation. Studies of the other pressure levels ≥200 mbar showed that the differences were not great (in accord with *Stolle et al.* [2009]).

### 2.2. The Data

[13] At the time of writing, the ECMWF interim reanalysis products were available from 1989 through 2009. The full reanalysis is on a T255 spherical harmonic grid corresponding to a resolution of about 0.7° (~79 km), and at 60 model levels. These levels are defined in a hybrid vertical coordinate system which are nearly sigma (terrain following) in the lower troposphere, becoming gradually more pressure-like in the higher levels. The publicly available products used here are on 1.5° latitude/longitude grids (corresponding to 166 km at the equator) and at 37 interpolated pressure levels (every 25 mbar in the lower troposphere). Although this is slightly lower than the full raw resolution it has the advantage of being less contaminated by the artificial hyperviscous dissipation used at the smallest scales (although there are still some dissipative effects as can be seen from the spectra). The reanalyses use a 4D var scheme to assimilate data with the help of the ECMWF numerical forecast model, details are provided by *Berrisford et al.* [2009].

[14] Of the 14 parameters available at the 700 mbar level (another 88 are available at the surface), we chose the temperature, specific humidity, zonal wind, meridional wind, vertical wind, and geopotential height (respectively: $T$, $h_s$, $u$, $v$, $w$, $z$) as being the most thermodynamically and dynamically important. Figure 1 shows the corresponding 0000 UT, 1 January 2006 fields. At (absolute) latitudes greater than 45°, the pixel size becomes markedly reduced. In addition, the data near the poles are much sparser for both the in situ and satellite data, so that we primarily focus on the region between ±45° latitude using a cylindrical projection. This has the advantage that to a reasonable approximation we can ignore the variation in pixel size and treat the data as coming from a Cartesian grid, analyzing and comparing exponents in the east-west and north-south directions using numerically convenient Fourier techniques (otherwise we should use spherical harmonics). In actual fact, the anisotropies in the statistics introduced by this limited map projection are of the order of a few percent only; see Appendix A for numerical and other details.

### 2.3. The Predictions of Multiplicative Cascade Models

[15] Cascades are generic processes that arise in nonlinear systems with large numbers of degrees of freedom. If there is a scale by scale conserved quantity (such as the energy

flux in hydrodynamic turbulence) and if the dynamical mechanism is scale invariant and if the main interactions are between neighboring scales, then one may expect the statistics to generally follow a (multi) scaling law of the type:

$$\langle \varphi_\lambda^q \rangle = \lambda^{K(q)}; \qquad \lambda = L/l \tag{1}$$

where "$\langle . \rangle$" indicates ensemble (statistical) averaging, $\varphi$ is the turbulent flux (e.g., the energy flux $\varepsilon$) normalized such that $\langle \varphi_\lambda \rangle = 1$, $K(q)$ is a convex function describing the scaling behavior of the $q$th moment, and $\lambda = L/l$ is the ratio of the (large) external scale $L$ (loosely speaking where the cascade starts), down to the scale of observation $l$. The flux is in Fourier space so that, for example, in the classical "direct" (i.e., large to small scale) and isotropic cascade, there is a quasi steady flux through spherical shells in Fourier space from low to high wave number. At small (dissipation) scales, the flux is equal to the dissipation and no longer propagates to smaller scales. More realistic cascades differ from this classical picture in several ways: (1) they are intermittent so that we expect at least occasional "backscatters," i.e., small to large scale fluxes, (2) as mentioned, the cascade is anisotropic due to gravity, the Coriolis force and boundary conditions, (3) the energy flux sources and sinks (chiefly short and long wave radiances) are themselves scaling so there is no classical source and sink free (pure) "inertial" range, and (4) in the horizontal, evidence is emerging that the cascade direction is not constant in time and place (e.g., aircraft data [*Lindborg*, 1999; *Lindborg and Cho*, 2001], scatterometer data (R. M. Kerr and G. P. King, Evidence for a midlatitude meso-scale downscale energy cascade from the marine boundary layer, http://www.docstoc.com/docs/70470043/Evidence-for-a-mid-latitude_-mesoscale-downscale-energy-cascade-), and ECMWF interim data [*Lovejoy and Schertzer*, 2011a]).

[16] Statistics following equation (1) are the generic outcomes of multiplicative cascade models in which large scale "parent" structures multiplicatively modulate the flux passed on to smaller "daughter" structures. One may already note that in the framework of generalized scale invariance (GSI), the scales $l$, $L$ are no longer required to be the usual (isotropic, Euclidean) scales [*Schertzer and Lovejoy*, 1985a]; therefore equation (1) is quite general potentially applying to highly stratified but scaling systems such as the atmosphere. For comparison, in the classical quasi-Gaussian (nonintermittent) turbulence model we have the trivial exponent $K(q) = 0$. In the analyses below, the ensemble is finite, not infinite and in the 1-D analyses we average over the remaining coordinates.

[17] Since the cascade is multiplicative, its logarithm is additive. It is therefore not surprising, although for a time it was debated [*Schertzer and Lovejoy*, 1997], that due to the additive central limit theorem for the sums of identical independently distributed random variables, there are specific (stable, attractive) "universal" forms for the exponent $K(q)$ [*Schertzer and Lovejoy*, 1987]:

$$K(q) = \frac{C_1}{(\alpha - 1)}(q^\alpha - q) \tag{2}$$

where $C_1$ is the "codimension of the mean," which characterizes the sparseness of the set that gives the dominant contribution to the first order statistical moment (the mean), and respects $0 \leq C_1 \leq d$, where $d$ is the dimension of the embedding space. The multifractal index $0 \leq \alpha \leq 2$ characterizes the degree of multifractality, i.e., the shape of the $K(q)$ function. It is also the Levy stability index of the cascade generator $\Gamma_\lambda = \log\varphi_\lambda$. If the cascade is unifractal/monofractal, then $\alpha = 0$, whereas $\alpha = 2$ corresponds to the "lognormal" multifractal (more precisely, its generator is Gaussian). A universal multifractal is termed "universal" because it is the basin of attraction for a wide variety of different multiplicative processes. In our analyses, we will see that the universal form (equation (2)) fits the empirical $K(q)$ quite well so that irrespective of whether the numerical models are indeed universal multifractals, the parameters $C_1$, $\alpha$ give very convenient parameterizations of their forms (although due to the interesting phenomenon of "multifractal phase transitions" [*Schertzer and Lovejoy*, 1992], this breaks down at large enough $q$; often not much higher than $q \approx 2 - 3$). In addition, irrespective of whether the cascades are exactly universal, $C_1$ and $\alpha$ still characterize, respectively, the sparseness near the mean and the curvature (and hence degree of multifractality) near the mean. In this paper we therefore often use $C_1$, $\alpha$ to reduce the characterization of the scaling (via the exponents $K(q)$) to manageable proportions (to two parameters). In any event, we show that the data fairly convincingly demonstrate a "Levy collapse" when the moments are normalized by the theoretical universal $K(q)$, and this even for scales at least somewhat outside the scaling range (see *Stolle et al.* [2009, submitted manuscript, 2011], *Lovejoy and Schertzer* [2010] and section 3.4 below). In other words, the universality relation equation (2) may be respected even when the scaling relation equation (1) holds with a nontrivial generalized scale, rather than with the usual (Euclidean) scale.

## 2.4. Estimating the Turbulent Fluxes From the Fluctuations

[18] In order to test equation (1), we must use an approach that does not require a priori assumptions about the physical nature of the relevant fluxes nor of their scale symmetries (isotropic or otherwise); the latter will in fact turn to out to be anisotropic and hence nonclassical. If atmospheric dynamics are controlled by scale invariant turbulent cascades of various (scale by scale) conserved fluxes $\varphi$ then in a scaling regime, the fluctuations $\Delta f(\Delta x)$ in an observable $f(x)$ (e.g., wind, temperature or radiance, $x$ is a coordinate (here, east west, north south or time) over a length $\Delta x$ are related to the turbulent fluxes by a relation of the form $\Delta f(\Delta x) = \varphi \Delta x^H$. This is a generalization from the classical turbulence laws: for example, the Kolmogorov law is the case when $\Delta f = \Delta v$ (velocity fluctuations), and for temporal fluctuations in a Lagrangian frame, $H = 1/2$, and $\varphi = \varepsilon^\eta$, $\eta = 1/2$, while for spatial fluctuations, we have $H = 1/3$ and $\varphi = \varepsilon^\eta$, $\eta = 1/3$. Similarly, the Corrsin-Obukhov law for fluctuations in a passive scalar ($\Delta f = \Delta\rho$) is recovered with $\varphi = \chi^{1/2}\varepsilon^{-1/6}$, $H = 1/3$ where $\chi$ is the passive scalar variance flux. Without knowing $\eta$ or $H$, nor even the physical nature of the flux, we can use this to estimate the normalized (nondimensional) flux $\varphi'$: a random field at the smallest resolution of our data:

$$\varphi' = \varphi/\langle\varphi\rangle = \Delta f/\langle\Delta f\rangle \tag{3}$$

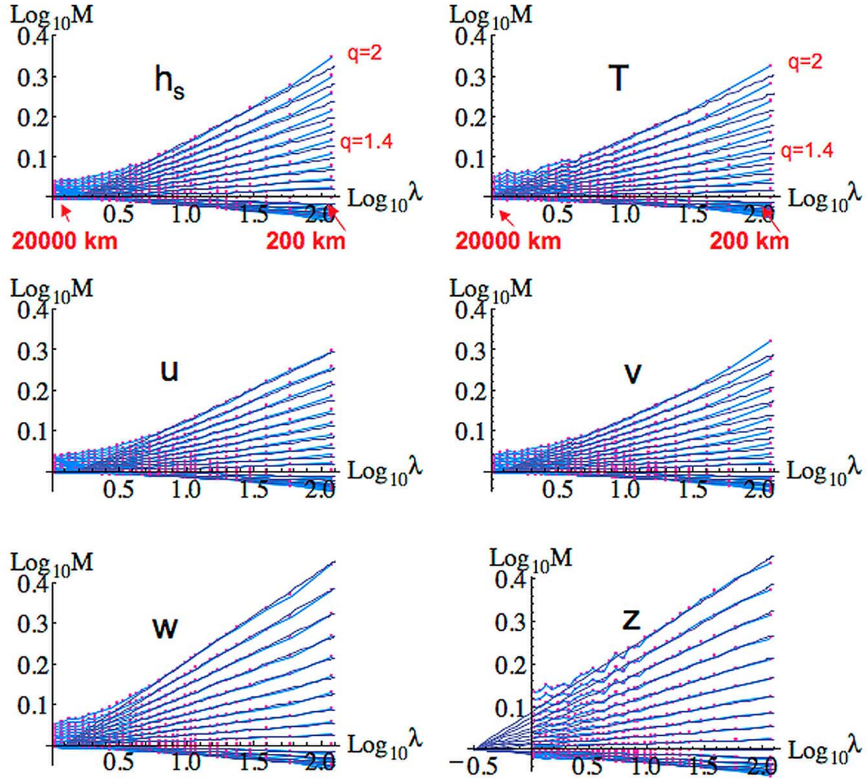

**Figure 2a.** The analysis of the 700 mbar fields at 0000 UT for 2006 between latitudes ±45°. The fluxes were estimated using finite difference Laplacians. The curves are the moments $q = 0, 0.1, 0.2, \ldots, 1.9$, and 2; $\lambda = 1$ corresponds to the size of the Earth, 20,000 km. The dots are the actual empirical values, and the straight lines are log-log regressions of equation (4) (i.e., with slopes $K(q)$) forced to go through a common point (the external scale ratio $\lambda_{eff}$).

Note that if the fluxes are realizations of pure multiplicative cascades then the normalized $\eta$ powers, $\varepsilon^{\eta}/\langle\varepsilon^{\eta}\rangle$, are also pure multiplicative cascades, so that $\varphi' = \varepsilon^{\eta}/\langle\varepsilon^{\eta}\rangle$ is a normalized cascade quantity.

[19] The fluctuation $\Delta f(\Delta x)$ can be estimated in various ways; for example with the help of the absolute first order finite difference: $\Delta f(\Delta x) = |f(x + \Delta x) - f(x)|$ or of a second order difference: $\Delta f(\Delta x) = |f(x) - (f(x + \Delta x) + f(x - \Delta x))/2|$ (we average over $x$ so that the statistics of $\Delta f$ are independent of $x$). These "poor man's wavelets" are adequate when, as is typically the case, $0 \le H \le 1$ (for first order differences) or $0 \le H \le 2$ (second order differences). If desired, other definitions of fluctuations (other wavelets) could be used. In order to analyze the fluxes over the widest range of scales possible, we take $\Delta x$ at the smallest resolution (1 pixel = 1.5° ≈ 170 km) and then obtain the intermediate resolution estimates of the flux by averaging (in space, in time). In the analyses below, we used second order differences in space using the (isotropic) spatial second finite difference i.e., the finite difference Laplacian obtained by taking the absolute difference between the value at a pixel and the mean of the four neighboring pixels (north, south, east, west). The resulting high resolution normalized flux estimates $\varphi'_{\Lambda} = \Delta f_{\Lambda}/\langle\Delta f_{\Lambda}\rangle$ can then be degraded (by averaging) to a lower resolution $L > L_i$ with scale ratio $\lambda = L_{ref}/L < \Lambda$ where $L_{ref}$ is a convenient reference scale (see below); $L_i$ is the smallest ("inner") pixel scale corresponding to largest scale ratio $\Lambda = L_{ref}/L_i$. For the reanalyses, this is a (hyper) viscous dissipation scale estimate since although it is not at the finest reanalysis resolution (0.7°, rather than the publicly available 1.5° resolution we use), the spectra show that they are still significantly influenced by the (hyper) viscous smoothing. Stolle et al. (submitted manuscript, 2011) compared the fluxes estimated from the spatial and the temporal second differences which are at intervals significantly different from the model integration time scales; they are in the model scaling regime (however, the use of different fluxes gave generally close results).

[20] Since empirically, the outer scale is not known a priori (it is an interesting parameter in its own right), we define scales with respect to a convenient reference scale; in space, we take $L_{ref}$ = 20000 km, and in time the external scale of the data set was used; $\tau_{ref}$ = 1 year. We then have:

$$M_q = \left(\frac{\lambda}{\lambda_{eff}}\right)^{K(q)}; \qquad \lambda_{eff} = L_{ref}/L_{eff} \tag{4}$$

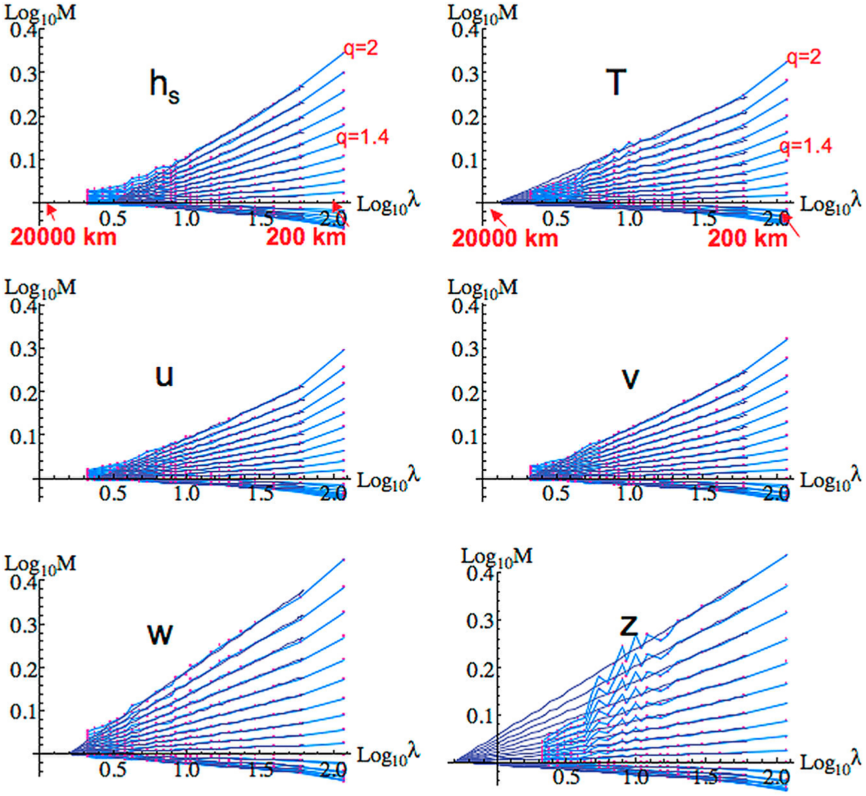

**Figure 2b.** Same as Figure 2a but for the meridional analysis. The data span 90° in latitude, i.e., 10000 km, but the reference scale was kept at 20,000 km as in Figure 2a.

where $L_{eff}$ is the effective outer scale of the cascade, $\lambda_{eff}$ the corresponding ratio and $M_q = \langle \varphi'^{q}_{\lambda} \rangle = \langle \varphi^{q}_{\lambda} \rangle / \langle \varphi_{\lambda} \rangle^{q}$ is the $q$th moment of the dimensionless normalized flux.

## 3. Cascade Analyses

### 3.1. The Basic Cascade Structures

[21] The basic cascade analyses are presented in Figure 2a (zonal), Figure 2b (meridional), and Figure 2c (time). In each case we start with the finite difference absolute Laplacian flux estimate which was then degraded by averaging in the corresponding direction and then averaged over the other directions. One can clearly see the basic cascade structure of lines converging to the external scales; note in particular that for the spatial analyses (Figures 2a and 2b) that the external cascade scales are systematically comparable to the largest great circle distance (20000 km), and that the scaling (i.e., the log-log linearity of the empirical points) is well respected at all but the largest scales (i.e., for $\log_{10}\lambda > \sim 0.6$ i.e., for scales $<\sim 5000$ km). The moments are only shown up to order $q = 2$ since for large enough $q$ they become dominated by the largest value present in the data sample so that the results spuriously depend on the sample size ($K(q)$ becomes spuriously linear; this is a "multifractal phase transition"). It was found that in this data, the transition always occurred for $q$ somewhat greater than 2, so that the moments shown here are well estimated from the data.

[22] In order to quantify the cascade statistics, we performed fits to the universal multifractal form (equation (2)). Since the results were found to vary little from zonal to meridional to time, rather than give separate tables of parameters for each, Table 1 gives the mean parameters with the direction to direction variations indicated by the "±"; these variations are apparently less than the systematic and statistical uncertainties. Two estimates of the $C_1$ parameter are given, one from the universal multifractal fit (i.e., with $K(q)$ constrained to the form equation (2)) and the other simply from the numerical derivative: $C_1 = K'(1)$; in both cases, the lines were constrained to pass through a single external scale since this is the prediction of the more fundamental equation (1). It can be seen that the $C_1$ estimates are very close, although the difference is generally larger than the direction to direction spread; we take this as evidence that the direction to direction differences (corresponding to possible space-time scaling anisotropy in the fluxes) are not statistically significant.

[23] In order to quantify the accuracy of the fits, we estimated the residuals as:

$$\Delta = \overline{\left| \log_{10}(M_q) - K(q)\log_{10}(\lambda/\lambda_{eff}) \right|} \qquad (5)$$

where the overbar represents averaging over all the moments $q \le 2$ and over the scale ratios larger than a critical value. In space, this was taken as the scale ratio corresponding to 5000 km, in time, it was the ratio corresponding to 8 days. The percentage deviation $\delta$ over the range is given in Table 1 and is estimated as $\delta = 100(10^{\Delta} - 1)$. From Table 1 we see that the typical accuracy is better than ±0.5% (the worst fit

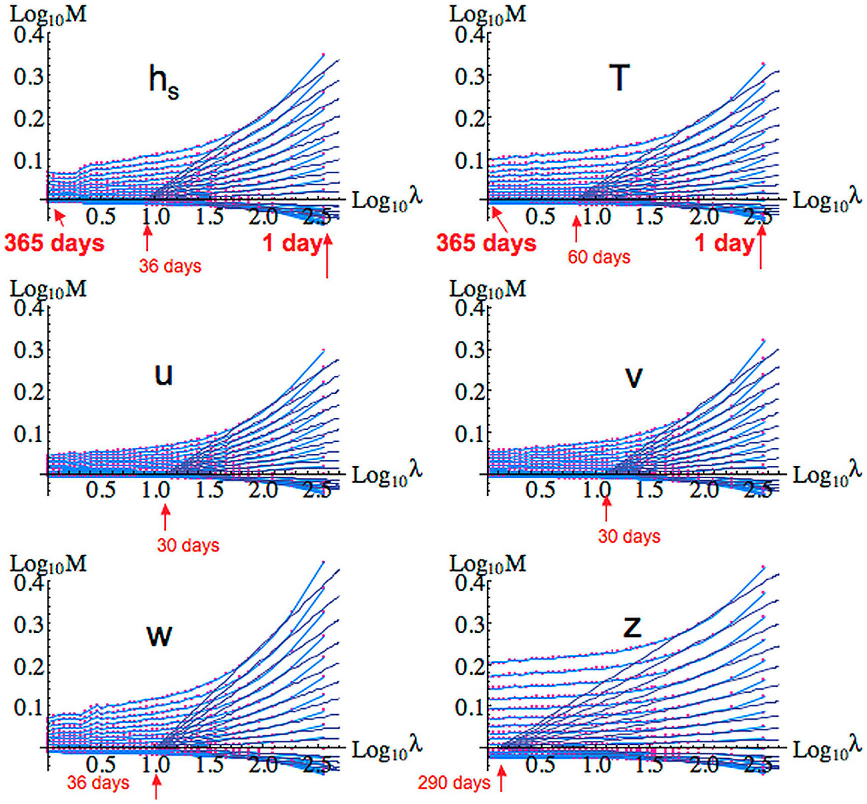

**Figure 2c.** Same as Figures 2a and 2b but for the temporal analyses; $\lambda = 1$ corresponds to 1 year. The effective outer temporal cascade scales ($\tau_{eff}$) are indicated with arrows.

was for the geopotential height in the meridional direction where it was ±0.9%). We may also note that all the different fields have very similar intermittency parameters: for the universal multifractal estimates, the $C_1$ vary only from 0.077 ($T$) to 0.121 ($w$) and $\alpha$ only from the lowest 1.77 ($h_s$) to the highest 1.92 ($w$). The most significant differences are for the external scales. Whereas the scaling exponent $C_1$ quantifies the mean variability (intermittency), for fixed $q$, changing the external scale changes $M_q$ at all scales by the same factor. Since the zonal and meridional $K(q)$ are very close, there is little scale by scale (differential, not absolute) horizontal anisotropy; however, the ratio of the zonal to meridional external scales is $1.6 \pm 0.3$ (the spread is from one of the six analyzed fields to the other) which indicates a strong "trivial," i.e., nonscaling, anisotropy so that typical isolines of flux are (roughly) elongated ellipsoids a scale-independent factor 1.6 longer in the zonal direction than in the meridional direction corresponding to the fact that the gradients of the fluxes (at each scale) are typically about 1.6 times stronger in the north-south direction. We return to this important anisotropy issue in section 3.2.

[24] Finally, it is of interest to compare the ECMWF interim to other model and reanalysis parameters published by *Stolle et al.* [2009] (spatial) and Stolle et al. (submitted manuscript, 2011) (temporal analyses). The latter restricted their attention to the zonal wind ($u$), temperature ($T$) and humidity fields ($h$). Considering the spatial (EW direction) analyses (Table 2a) we see that the parameters are very close to those of the other products although the $C_1$ parameter is systematically a little smaller while the outer scales are systematically a little larger. At any scale these two effects will tend to cancel since a smaller $C_1$ indicates that starting at the external scale, the variability builds up more slowly for the ECMWF interim; however there is an overall increase in the outer scale so that this lower scale by scale variability builds up over a wider range. In Table 2a we also show estimates from in situ aircraft measurements which include various efforts to minimize the biases introduced by the aircraft trajectories (intermittent fractality as well as from the effects of nonzero slopes).

[25] The temporal cascade parameters are indicated in Table 2b. Once again we see that, although the parameters from the different products are not very different, the $C_1$ values are systematically lower for the ECMWF interim reanalyzes whereas the external scales ($\tau_{eff}$) are systematically larger. In this case, however, the $\tau_{eff}$ values are often several times larger indicating that the actual variability of the ECMWF interim is much larger. If instead of the effective outer scale (where the lines converge), we consider the scale at which the lines start to significantly deviate ($\tau_{trans}$) ("trans" for "transition") from the empirical moments, then the difference is not so large: about 8 days in all cases (see Stolle et al. (submitted manuscript, 2011) for more systematic discussion of this). In the latter paper, it was argued that $\tau_{trans}$ marks the beginning of the transition from weather to climate, that $\tau_{eff}$ marks the end of the transition range and that the scales $>\tau_{eff}$ are in a "pure" climate regime: see Table 2b and Figure 2c.

**Table 2a.** The East-West Analysis of the Fluxes Obtained as the Laplacians[a]

| | ECMWF Interim | ERA40 | 20th Century | GEM | GFS | Aircraft |
|---|---|---|---|---|---|---|
| | | | $u$ | | | |
| $\alpha$ | 1.86 | 1.93 | 1.87 | 1.68 | 1.80 | 1.94 |
| $C_1$ | 0.081 | 0.096 | 0.089 | 0.104 | 0.082 | 0.088 |
| $L_{eff}$ | 12700 | 12000 | 16000 | 11000 | 9000 | 25000 |
| | | | $T$ | | | |
| $\alpha$ | 1.89 | 2.11 | 1.85 | 1.94 | 2.00 | 1.78 |
| $C_1$ | 0.074 | 0.094 | 0.088 | 0.077 | 0.080 | 0.107 |
| $L_{eff}$ | 20000 | 14500 | 16000 | 8300 | 8600 | 5000 |
| | | | $h_s$ | | | |
| $\alpha$ | 1.70 | 1.75 | 1.73 | 1.60 | 1.74 | 1.81 |
| $C_1$ | 0.095 | 0.094 | 0.077 | 0.100 | 0.091 | 0.083 |
| $L_{eff}$ | 12700 | 11000 | 50000 | 11800 | 9000 | 10000 |

[a] Fluxes: the ECMWF interim data from Figure 2a, the Twentieth Century reanalysis (1871–2008, every 6 h, 2° resolution, 44–46° N only) [*Lovejoy and Schertzer*, 2011a], and the others from *Stolle et al.* [2009]. Data are from ±45° latitude, 700 mbar. The aircraft data are from *Lovejoy et al.* [2010] and have been corrected by the factor $(3/2)^\alpha \approx 2.07$ which is a theoretical estimate of the difference between the dissipation scale flux estimates and the scaling range flux estimates. Also, they are for roughly 200 mbar flight levels rather than 700 mbar levels (but the model parameters did not change too much as functions of altitude). Note that the $L_{eff}$ for the wind is probably too big due to turbulent intermittency effects of the aircraft trajectory; see *Lovejoy et al.* [2010] for discussion.

### 3.2. Space-Space and 1Space-Time Diagrams

[26] *Lovejoy and Schertzer* [2010] pointed out that the planetary scale scaling of the horizontal wind allows the Kolmogorov law to operate up to these scales so that the energy flux plays a fundamental role. This was estimated from first principles starting with the solar flux at the top of the atmosphere and assuming (1) a mean ≈20% albedo, (2) a 2% efficiency of conversion to kinetic energy, and (3) that the flux is distributed more or less uniformly throughout the troposphere. The result, $\varepsilon \approx 5 \times 10^{-4}$ m$^2$/s$^3$ was close to the direct estimates form ECMWF interim reanalyses ($\varepsilon \approx 10^{-3}$ m$^2$/s$^3$), and predicts that structures of size $l$ have lifetimes ("eddy turnover times") $\tau \approx \varepsilon^{-1/3} l^{2/3}$ of structures. The critical weather-low-frequency weather transition time scale ($\tau_w$) is therefore $\tau_w = \tau_{eff} = \varepsilon^{-1/3} L_{eff}^{2/3} \approx$ 10 days and $V_{eff} \approx \varepsilon^{1/3} L_{eff}^{1/3}$ 20 m/s (using the planet scale 20000 km to estimate $L_{eff}$; see below for latitudinal dependent refinements). For scales $\tau > \tau_w$, the spatial degrees of freedom become rapidly quenched so that the long time variability is increasingly dependent only on temporal interactions rather than space-time interactions; the statistics undergo a "dimensional transition" [*Lovejoy and Schertzer*, 2010].

[27] To directly study the space-time cascade relations, we can use the cascades to construct space-space and space-time diagrams, therefore to infer the relevant generalized space-time scale. This is possible because, for example, comparing spatial and temporal statistics, we can define space-time relations using the following implicit relation between length scales $L$ and time scales $\tau$:

$$\left\langle \phi^q_{L_{ref}/L} \right\rangle = \left\langle \phi^q_{\tau_{ref}/\tau} \right\rangle \qquad (6)$$

[28] Actually, equation (6) gives a different relation between $L$ and $\tau$ for each $q$ value. However, in the simplest GSI case where the $C_1$ and $\alpha$ for the spatial and temporal analyses are the same (as is roughly the case here, see Table 1), any $q$ will give the same relationship although larger values of $q$ will give more statistically accurate results (as long as the moments are not so large as to be spuriously dependent on a few extreme values and the value $q = 1$ does not work since the corresponding moments are independent of scale). Here we chose $q = 2$ which has the advantage that the corresponding $K(2)$ is precisely the intermittency correction necessary for the spectrum (which is a second order statistic); this is needed below. Figure 3 shows the results for $q = 2$ for the three pairs of directions: NS/EW, EW/time, NS/time. The space-time diagrams show that a linear (constant velocity) relation between space and time works reasonably well up to 2000–2500 km in space and up to time scales of ~7–10 days in time. After 7–10 days there is a drastic change in the relationship; this is the transition to the low-frequency weather regime. While the space-space diagram shows that structures are typically elongated in the EW direction by factors up to about 1.6 comparable to the value of the (average) $L_{eff,EW}/L_{eff,NS}$ ratio discussed above, the space-time diagrams indicate effective space-time transformation speeds $V_{eff} = L_{eff}/\tau_{eff}$ in the range ~200–400 km/d (~2.5 to 5 m/s).

### 3.3. Latitudinal Dependence

[29] Up until now, we have taken statistics from ±45° latitude in order to concentrate on the basic variation with direction (zonal, meridional, temporal). However, a basic aspect of atmospheric dynamics is its latitudinal dependence, notably due to the Coriolis force and strong north-south temperature gradients. Paradoxically, the fairly limited analysis of latitudinal dependence by *Stolle et al.* [2009] found that latitudinal variations were small; this is presumably because the cascade structure is mostly dependent on the nonlinear interactions whereas the most important north-south effects involve linear terms and boundary conditions. Let us now investigate this more systematically here.

[30] In order to study the latitudinal dependence, we broke up the Earth into 15° bands: Figure 4a shows the moments for the $\theta$ = 0–15°N band, and Figure 4b shows the 45–60°N band. The main differences visible are small but systematic

**Table 2b.** The Temporal Analysis of the Fluxes[a]

| | ECMWF Interim | ERA40 | 20th Century | GEM | GFS |
|---|---|---|---|---|---|
| | | $u$ | | | |
| $\alpha$ | 1.83 | 1.7 | 1.81 | 1.8 | 1.8 |
| $C_1$ | 0.091 | 0.10 | 0.083 | 0.12 | 0.11 |
| $\tau_{eff}$ (days) | 29 | 7 | 16 | 13 | 5 |
| | | $T$ | | | |
| $\alpha$ | 1.90 | 1.9 | 1.82 | 2.0 | 1.8 |
| $C_1$ | 0.082 | 0.10 | 0.090 | 0.12 | 0.13 |
| $\tau_{eff}$ (days) | 58 | 9 | 13 | 28 | 82 |
| | | $h_s$ | | | |
| $\alpha$ | 1.83 | 1.7 | 1.74 | 1.6 | 1.7 |
| $C_1$ | 0.098 | 0.12 | 0.083 | 0.14 | 0.12 |
| $\tau_{eff}$ (days) | 46 | 9 | 40 | 12 | 13 |

[a] ECMWF interim, 20th century, 24 h time resolution (from Figure 2c, obtained from Laplacians), and for the others (6 to 12 h resolutions) from the second time derivative, these are reproduced from Stolle et al. (submitted manuscript, 2011). All the data are from ±45° latitude, 700 mbar (except 20th century which is only 44°N–46°N).

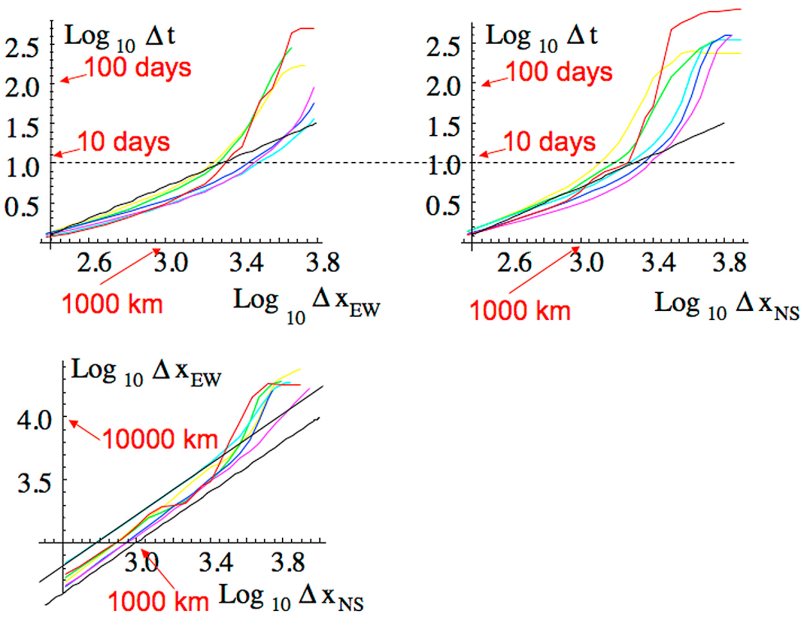

**Figure 3.** Space-time and space-space plots using the $q = 2$ moments and using $\lambda = \tau_{ref}/\Delta t$ and $\lambda = L_{ref}/\Delta x$ for time and space, respectively; (top left) east-west and time, (top right) north-south and time, and (bottom left) north-south and east-west. Yellow is $h_s$, green is $T$, cyan is $u$, blue is v, purple is $w$, and red is $z$. In all cases, the black reference lines have slopes 1; in the space-time diagrams, it corresponds to a speed of ≈225 km/d; the spread in the lines indicates a variation over a factor of about 1.6 in speed. In the space-space diagram the bottom reference line corresponds to isotropy; the top corresponds to an aspect ratio of ≈1.6 difference as discussed in the text.

changes in the outer scales. The same data in the time domain is shown in Figures 4c and 4d. The variation is pretty small and is confirmed in the other bands (not shown). Also, for the exponents, there is generally a good degree of north-south symmetry. In order to quantify this, we turn to Figures 5a and 5b which show the evolution of the exponents $C_1$, $\alpha$ (Figure 5a), and the external spatial and temporal scales (Figure 5b). First for a given field, we can compare the space and time exponents; we find the differences are generally less than 0.02 for $C_1$ and less than 0.1 for $\alpha$, which is probably less than the statistically significant level, especially since the sample size of each 15° band is 1/6 of the previously analyzed (90°) band, and the range of scaling in the time domain was quite limited (2–8 days; the 1 day value was not used since, as can be seen from the plots, it suffers from "finite size effects"). In addition, we see that for some of the fields (essentially the geopotential and specific humidity near the equator), the $\alpha$ values are a bit larger than the theoretical maximum (= 2) so that the curvature ($\alpha$) estimates (which were made here using $\alpha = K''(1)/K'(1)$) are not too accurate; their deviations from $\alpha = 2$ are probably not statistically significant. We notice a slight tendency for the intermittency to increase away from the equator, especially in the southern hemisphere; it is sufficiently systematic that it is probably a real change in $C_1$.

[31] Even though the exponents show remarkably little latitudinal variation, that does not imply that the cascade structure is nearly independent of latitude. Figure 5b shows the variation of the external space and time scales as well as their ratios, the effective speed $V_{eff}$ needed for space-time transformations. The main noteworthy features are: (1) The latitudinal variations in external scales are relatively small (except perhaps for the geopotential height); in space they are almost all between 10,000 and 20,000 km, in time between 20 and 40 days, and in speed, between 400 and 1000 km/d. (2) The external scales have significant north-south asymmetry, especially the time scales of the northern hemisphere which have significantly larger $\tau_{eff}$; however this is somewhat mirrored in larger $L_{eff}$ values so that their ratio ($V_{eff}$) drops in the northern hemisphere. The reason for the asymmetry is not clear and it may be partly due to factors such as differences in data density and land cover between the two hemispheres. Using the observed $L_{eff}(\theta)$ and the observed latitudinally varying $\varepsilon(\theta)$ from the same reanalyses [see *Lovejoy and Schertzer*, 2010], we can theoretically estimate $\tau_{eff}(\theta) = \varepsilon(\theta)^{-1/3}L_{eff}(\theta)^{2/3}$ and $V_{eff}(\theta) = \varepsilon(\theta)^{1/3}L_{eff}(\theta)^{1/3}$. For the published range of $\varepsilon(\theta)$ ($-45° < \theta < 45°$), these theoretically predicted curves are superposed against the empirical curves (Figure 5b). We see that the pattern of latitudinal variations of $\tau_{eff}$ and $V_{eff}$ are very close to those predicted on the basis of the mean latitudinal energy flux $\varepsilon(\theta)$ but there is an offset of factor ~1.6.

### 3.4. Levy Collapse: Generalized Scale Invariance in the Low-Frequency Weather Regime

[32] We found that the universal multifractal form (equation (2)) leads to good fits over all the moments (up to $q = 2$) and scales up to 5000 km and 7–10 days in time, after which the scaling breaks down. However, as discussed above, a space-time cascade model of the atmosphere predicts a break ("dimensional transition") at the weather scale $\tau_w \approx 10$ days. By extending the stochastic cascade model

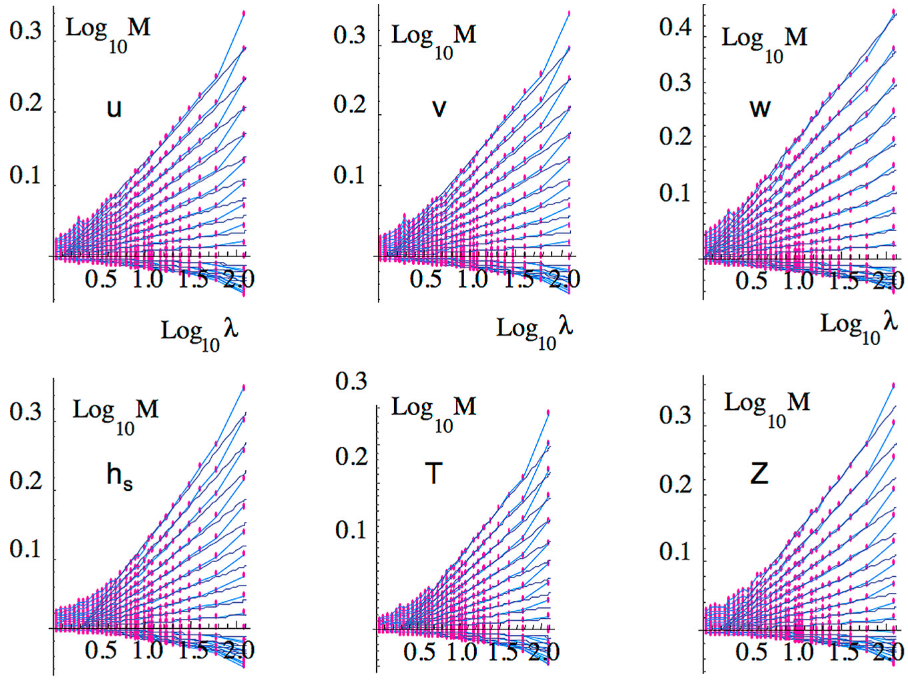

**Figure 4a.** The cascade analyses of the (absolute) spatial finite difference Laplacian from the band 0°–15°N, zonal analysis; external reference scale = 20,000 km (corresponding to $\lambda = 1$). The moments used are $q = 0.1, 0.2, \ldots, 1.9, 2.0$. The different fields are indicated in the plot ($u$, zonal wind; $v$, meridional wind; $w$, vertical wind; $h_s$, specific humidity; $T$, temperature; $z$, geopotential height). The straight lines are log-log regressions of equation (4) (i.e., with slopes $K(q)$) forced to go through a common point (the external scale ratio $\lambda_{eff}$).

that generates the “weather” to scales $\tau \gg \tau_w$, *Lovejoy and Schertzer* [2010] showed that the energy flux $\varepsilon$ can be written as a product of high-frequency space-time weather regime flux $\varepsilon_w(\underline{r}, t)$ multiplied by a low-frequency weather-low-frequency weather process $\varepsilon_{lw}(t)$ which is only a function of the total range of time scales longer than $\tau_w$. Theory shows that $\varepsilon_{lw}(t)$ has a asymptotically singular autocorrelation function $\langle \varepsilon_{lw}(t)\varepsilon_{lw}(t-\tau)\rangle \approx \tau^{-1}$ which implies a

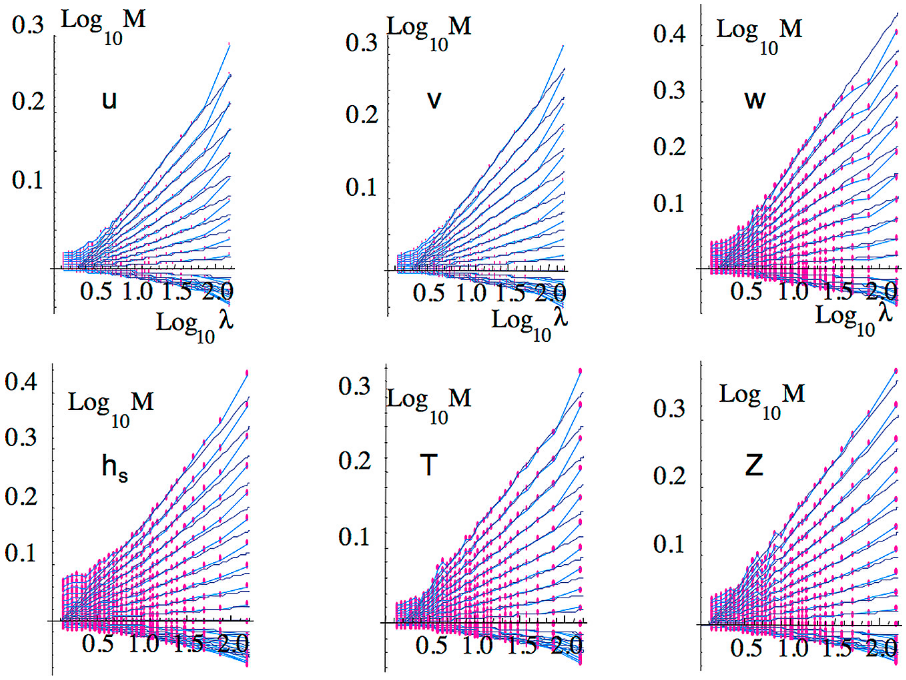

**Figure 4b.** Same as Figure 4a but for the band 45°N–60°N (zonal analysis).

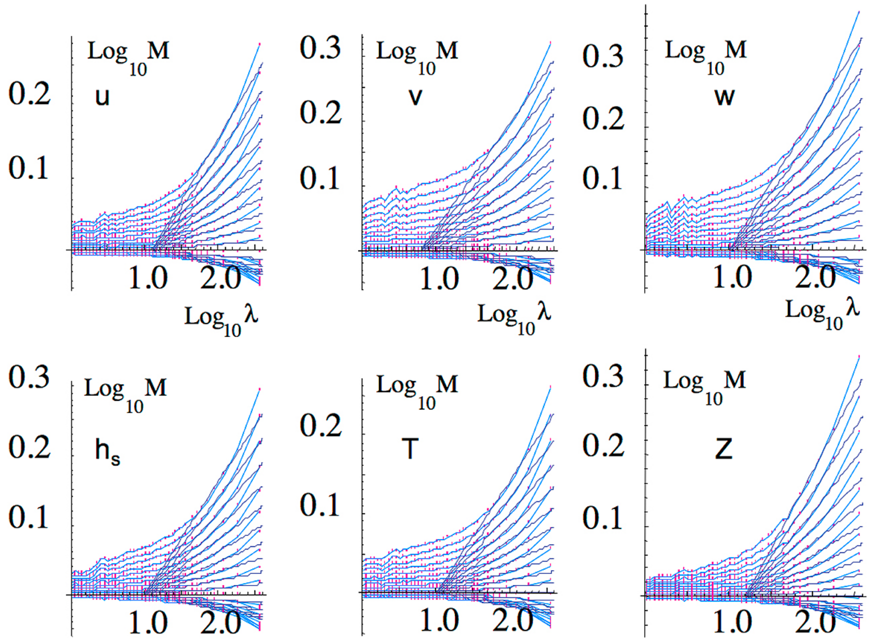

**Figure 4c.** Same as Figure 4a (the band 0°–15°N) but for the temporal analysis. The outer scale is 1 year (corresponding to $\lambda = 1$).

large $\tau$ divergence in the spectrum. In practice this means that the spectrum $E(\omega)$ for frequencies lower than $\tau_w^{-1}$ will have spectral exponent $\beta$ which depends only the outer scale (and weakly on $\alpha$) with realistic values in the range $\beta \approx$ 0.2–0.4 (with $E(\omega) \approx \omega^{-\beta}$; this reproduces the observed spectral plateau [see *Lovejoy and Schertzer*, 2011a]).

[33] Further consequences of the dimensional transition at $\tau_w$ are that although the "bare" $\varepsilon_{lw}(t)$ process (i.e., constructed down to a given scale and stopped) has roughly ("long tailed") log-Levy distributions, when, as in our data analysis, the process is continued down to much smaller scales and then averaged, the resulting "dressed" statistics will eventually be ("short tailed") quasi Gaussian. Therefore the Levy collapse is not expected to continue to time scales much longer than $\tau_w$. However, as discussed by *Lovejoy and Schertzer* [2011a] and mentioned in section 1, this pure atmosphere model does not take into account interactions with the oceans which apparently have similar turbulence and transitions, only with $\varepsilon_o \approx 10^{-8}$ m$^2$/s$^3$ and hence critical time scale $\tau_o \approx \varepsilon_o^{-1/3} L_e^{2/3} \approx 1$ year. The interaction between

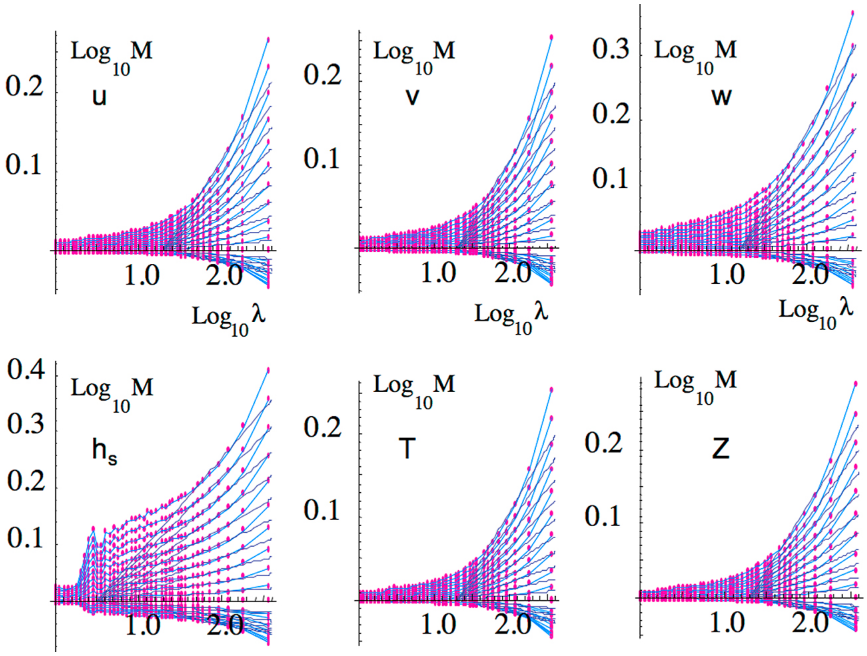

**Figure 4d.** Same as Figure 4b (the band 45°N–60°N) but for the temporal analysis.

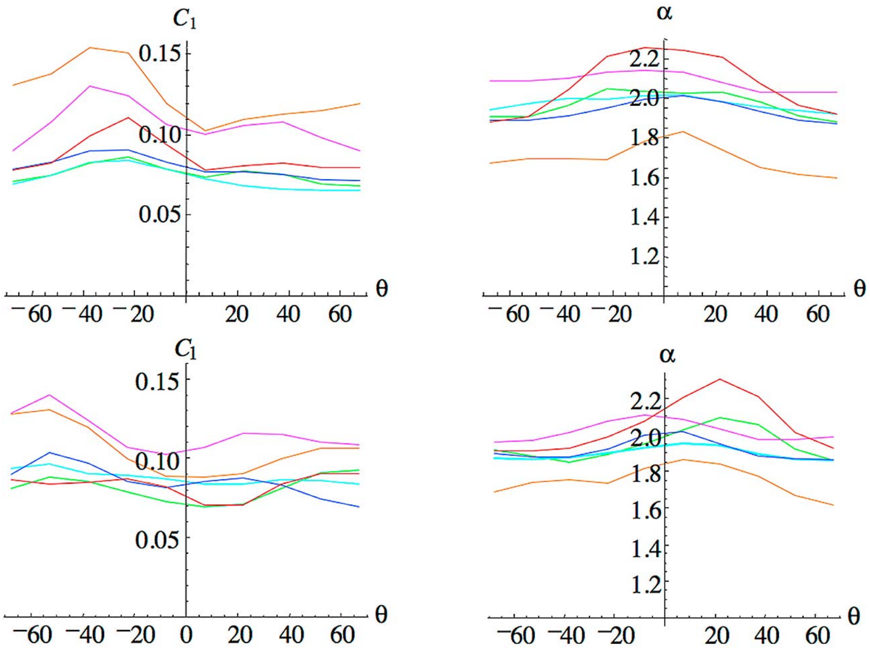

**Figure 5a.** The cascade exponents $C_1$ and $\alpha$ (top) from the spatial (zonal) analysis and (bottom) from the temporal analysis. From bottom to top in the top left plot, we have the zonal wind ($u$, cyan), the meridional wind ($v$, blue), the temperature ($T$, green), the geopotential height ($z$, red), the vertical velocity ($w$, purple), and the specific humidity ($h_s$, orange). The extreme latitude bands (±75°–90°) were not used since the mean map factor is very large and the results were considered unreliable.

the ocean and the atmosphere may therefore provide the extra correlations needed to allow the log-Levy distributions to continue to longer time scales of the order of one year.

[34] One way to check the log-Levy form of the probability distribution (both in the scaling range and beyond) is to consider the reduced moments:

$$M_q' = M_q^{(\alpha-1)/(q^\alpha - q)} \tag{7}$$

If an $\alpha$ index can be found such that these are independent of $q$ then the probabilities are log-Levy with corresponding $\alpha$ index. Figures 6a, 6b, and 6c show the results when $\alpha$ = 1.9 was used throughout (roughly the mean $\alpha$ value found from the regressions; see Table 1). In the scaling regime, all the moments "collapse" onto a single straight line: $M_q' = \lambda^{C_1}$; however, we see that even in the regime where $M_q'$ is no longer a power law with respect to time and/or space for large separations ($\lambda$), the curves continue to collapse indicating that they remain of the multifractal universality form. This collapse shows that $M_q'$ could be used to define a "generalized scale" $\lambda' = M_q'^{1/C_1}$ in the framework of extreme nonlinear GSI [*Schertzer et al.*, 1997] (any positive power of $\lambda'$ is acceptable). The degree of collapse can be simply judged by inspecting the bunching of the lines for different $q$ on top of each other: this can also be quantified scale by scale. For example, even at low $\lambda$ (i.e., at $\tau$ = 1 year), for the temporal cascades for $h_s$ and $T$ the collapse is only to within ±30% whereas also at one year, it is much better (±3%) for $u$ and $v$, ±6% for $w$ and still reasonable (±12%) for $z$. Similarly, in the east-west direction the spreads of the lines for different $q$ values at 20000 km are: ±10%, ±1.5%, ±6%, ±6%, ±10%, and ±10% for $h_s$, $T$, $u$, $v$, $w$, and $z$, respectively. Note that the spreads are large for the extreme small scale (one pixel in space, one day in time); this is presumably a finite size effect: the problem of convergence to an accurate flux estimate. These collapses thus give evidence that, presumably due to the effects of "ocean weather" on the atmosphere, the multiplicative structure of the fluxes continues even well into the climate regime.

## 4. The Scaling of the Fields and Spectra

### 4.1. Horizontal Anisotropy

#### 4.1.1. Generalized Scale Invariance

[35] Up until now, we have simply used the fields to define fluctuations at the smallest scales and hence to estimate the normalized turbulent fluxes. Since the fields are related to the fluxes by relations of the form $\Delta v = \varphi \Delta x^H$, we see that a full characterization of the statistics of the field $v$ requires the additional exponent $H$. For example, in the classical Kolmogorov scaling, $v$ is a velocity component $\varphi = \varepsilon^{1/3}$ where $\varepsilon$ is the energy flux to smaller scales and $H$ = 1/3. Taking the $q$th power and then the ensemble average of this relationship, we obtain:

$$\langle (\Delta v(\Delta x))^q \rangle = \langle \varphi_{\Delta x}^q \rangle \Delta x^{qH} = \Delta x^{\xi(q)}; \qquad \xi(q) = qH - K(q); \quad \Delta x \propto \lambda^{-1} \tag{8}$$

where $\xi(q)$ is the structure function exponent. From the Wiener-Khinchtin theorem, the power spectrum is the Fourier transform of the autocorrelation function. Since the second order structure function is to within a constant the same as the autocorrelation function, we obtain $E(k) \approx k^{-\beta}$

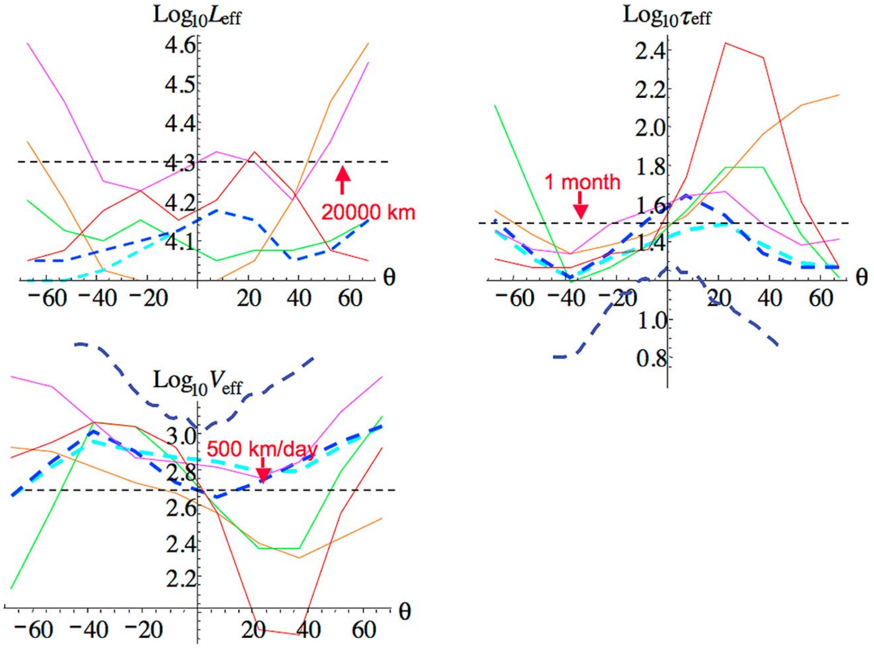

**Figure 5b.** The external scales as functions of latitude: (top left) the outer space scale (in units of kilometers) from the zonal cascade analyses and (top right) from the time analysis (in units of days), and (bottom left) their ratio, the effective speed of space-time transformations (in units of km/d). The dashed lines are convenient reference lines; note that 500 km/d = 5.8 m/s. The thick dashed blue and cyan lines are zonal and meridional wind components, respectively; in the $\tau_{eff}$, $V_{eff}$ plots we also show a short (between ±45° only) thick dashed dark blue line representing the theoretical predictions based on the latitude dependence of the tropospheric averaged $\varepsilon$ estimates from the ECMWF interim reanalyses estimated by *Lovejoy and Schertzer* [2010] using the zonal gradient estimates appropriate to these zonal analyses. As can be seen, the latitudinal variation is nearly exactly reproduced but the values are shifted by a factor $\approx 10^{0.2} \sim 1.6$.

with $\beta = \xi(2) + 1 = 1 + 2H - K(2)$. One can thus estimate $H$ from $K(2)$ and the Fourier domain scaling exponent $\beta$. However, in this case, the usual method, using isotropic spectra to estimate $\beta$, needs to be examined carefully. In addition, in the usual structure function the fluctuation $\Delta v$ is defined using the "poor man's" wavelet, i.e., simply a difference, in which case equation (8) is only valid for $0 < H < 1$ (the range of $H$ values can be extended using other wavelets to define $\Delta v$).

[36] Consider a field $f(\underline{r})$ where $\underline{r}$ is a position vector (extensions to space-time are straightforward). Define its Fourier transform (indicated by the tilda):

$$\widetilde{f(\underline{k})} = \int e^{i\underline{k}\cdot\underline{r}} f(\underline{r})\, d\underline{r} \qquad (9)$$

where $\underline{k}$ is the wave vector dual to $\underline{x}$. We can now define the power spectral density $P$:

$$P(\underline{k}) = \left\langle \left| \widetilde{f(\underline{k})} \right|^2 \right\rangle \qquad (10)$$

As before, the angle brackets mean "statistical averaging" and the vertical bars indicate the modulus of the complex $\widetilde{f}$. Here, the continuous transform is estimated using discrete fast Fourier techniques (with Hann windows), and the ensemble average is estimated by averaging over all the available data as discussed in section 2.1.

[37] If the system is statistically isotropic, then $P$ only depends on the vector norm of $\underline{k}$: $P(\underline{k}) = P(|\underline{k}|)$. Now consider an isotropic "zoom" (i.e., a standard "blow up") by factor $\lambda > 1$ in Fourier space: $\underline{k} \rightarrow \lambda\underline{k}$, equivalent to the physical space inverse "blow down": $\underline{r} \rightarrow \lambda^{-1}\underline{r}$. If the system is "self-similar," i.e., if it is both isotropic and also scaling, then the condition that the smaller scale is related to the larger scale without reference to characteristic size (i.e., that it is "scaling") implies the following power law relation between large scales $\lambda^{-1}|\underline{k}|$ and smaller scales $|\underline{k}|$:

$$P\left(\lambda^{-1}|\underline{k}|\right) \approx \lambda^{s} P(|\underline{k}|) \qquad (11)$$

The solution to the functional equation (11) is the following scaling law for $P$:

$$P(\underline{k}) \approx |\underline{k}|^{-s} \qquad (12)$$

We have deliberately proceeded step by step since we will shortly generalize this to non-self-similar, anisotropic scaling systems where the norm of $\underline{k}$ is replaced by a scale function which respects anisotropic scaling symmetries rather than the isotropic ones respected by the vector norm and the

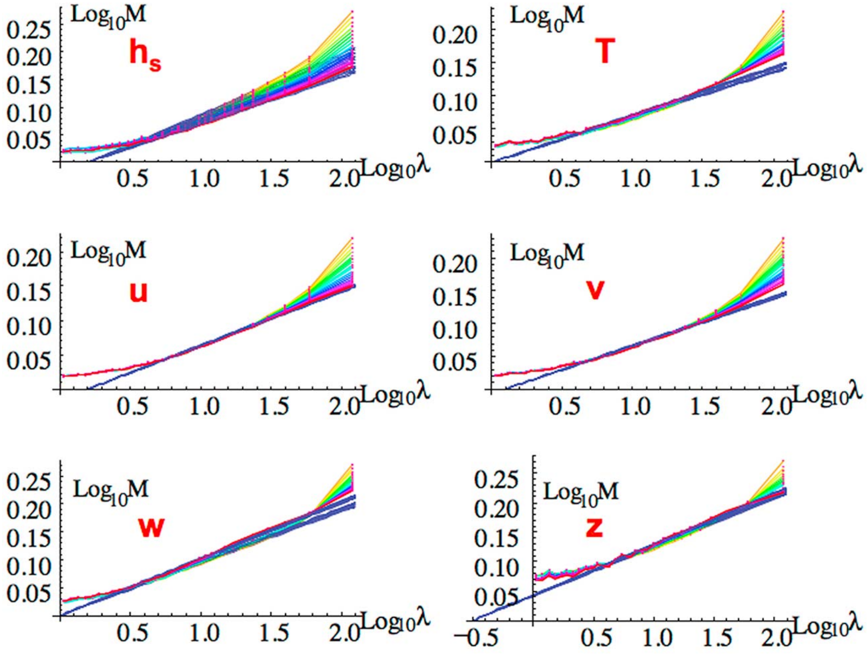

**Figure 6a.** The zonal analysis of the Levy collapse. The vertical scale is $\log_{10}M'_q$ (equation (7)). The value of $\alpha$ used in all the collapses was $\alpha$ = 1.9.

isotropic reduction $\lambda^{-1}$ is replaced by a more general anisotropic scale changing operator.

[38] It is now usual to introduce the "isotropic spectrum" $E(k)$ (with $k = |\underline{k}|$) obtained by integrating over all directions: in 1-D, $E(k) = 2P(k)$, in 2-D, $E(k) = 2\pi kP(k)$ and in 3-D, $E(k) = 4\pi k^2P(k)$. In terms of data analysis, where one has a finite rather than infinite sample size, one can profit from the angle integration to improve the estimate of $E(k)$ (to reduce the noise), by using:

$$E(k) = \int_{\delta S_k} P(\underline{k}')d\underline{k}' \tag{13}$$

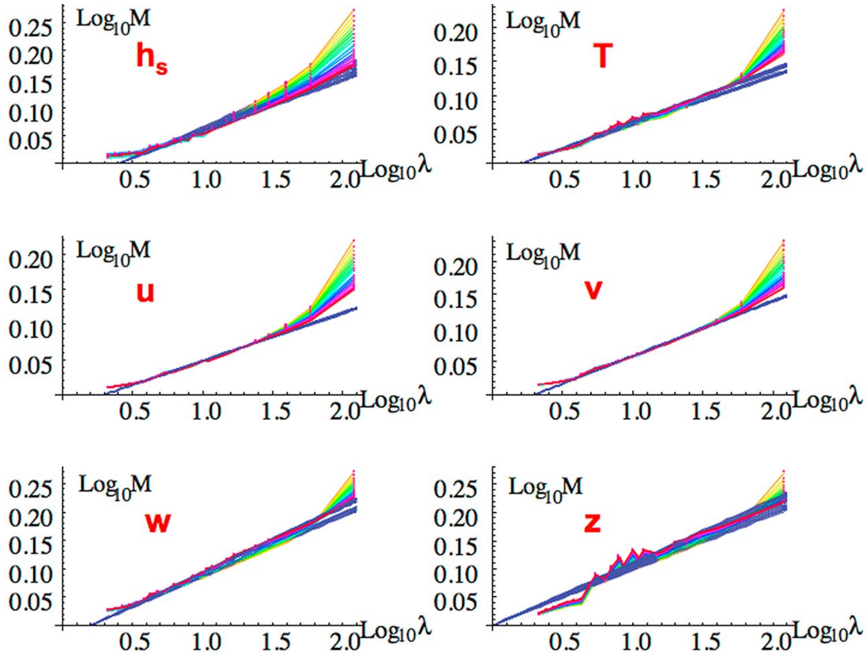

**Figure 6b.** Same as Figure 6a but for the meridional direction. The value of $\alpha$ used in all the collapses was $\alpha$ = 1.9.

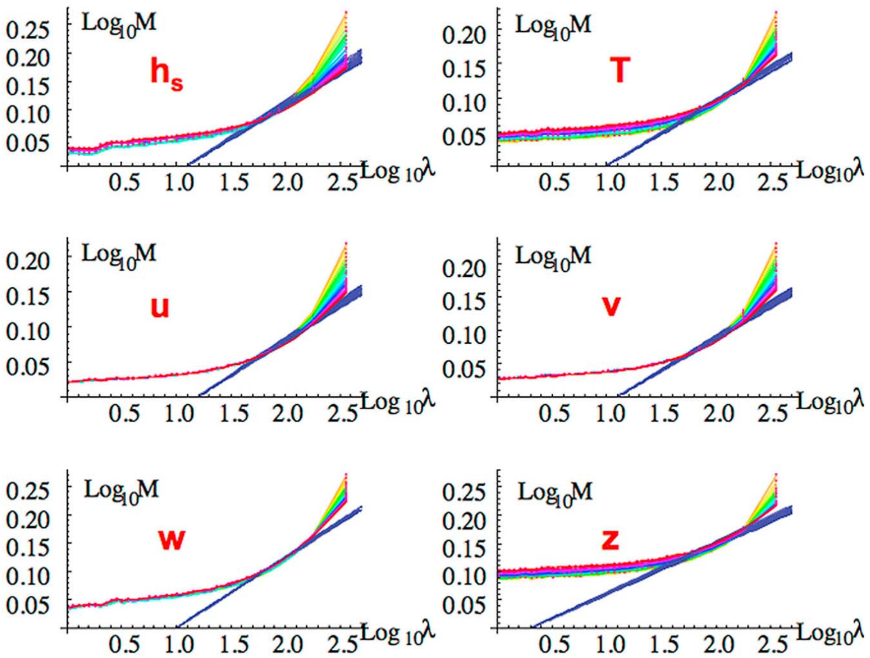

**Figure 6c.** Same as Figures 6a and 6b but for the temporal analysis of the collapse. The value of $\alpha$ used in all the collapses was $\alpha$ = 1.9.

where $S_k$ is the $d$-dimensional sphere and $\delta S_k$ is its boundary: in $d = 1$ it is the end points of the interval from $-k$ to $k$, in $d = 2$, it is the circle radius $k$, and in $d$ = 3, the spherical shell radius $k$ (in 1-D this just reduces to $E(k) = 2\langle|\widetilde{f(k)}|^2\rangle$). Using equation (13), we therefore take the power law dependence of the spectrum:

$$E(k) \approx k^{-\beta}; \qquad \beta = s - d + 1 \tag{14}$$

as evidence for scaling of the field $f$.

### 4.1.2. Testing GSI on Horizontal Reanalyses

[39] To estimate the spectrum on the reanalyses recall that in data analysis, the isotropy of $P$ is almost always simply assumed without question and $E(k)$ estimated by equation (13). However, a real problem arises because before interpreting the result, we ought first to check that $P(\underline{k})$ is indeed (nearly) isotropic, and this is rarely done. While, ideally, spherical harmonics should be used for spherical data, unfortunately there is no simple or obvious way to use them to study zonal versus meridional anisotropy. We thus resorted to using cylindrical maps and standard (Cartesian coordinate) Fourier techniques. We proceeded as follows: first, since the largest east-west distance is 180°, each latitudinal band from −45° to + 45° was broken into two longitudinal sections, one from 0 to 180° and the other from 180 to 0° longitude i.e., each 180° × 90° or 20000 × 10000 km or 120 × 60 reanalysis pixels (as usual, all spectra used Hann windows to reduce spectral leakage). Although it might at first sight appear that the use of this cylindrical map projection might in itself lead to a significant statistical anisotropy, the actual bias in the spectral density turns out to be very small. For example, in Appendix A we use numerical simulations to study the effect of the mapping in detail; a brief summary follows. While the effect of the map projection increases with $H$, we find that over the relevant empirical range $0.33 < H < 1.25$, that the spectral density $P$ (which varies by more than 4–5 orders of magnitude) is only affected by a few percent. Even with the largest value $H$ = 1.25 (for the geopotential height), the zonal and meridional spectral exponents are only biased by, respectively, $\Delta\beta \approx 0.01$, $\Delta\beta \approx 0.05$, which is much smaller than the empirically estimated difference $\Delta\beta \approx 0.5$ between the meridional and the zonal geopotential value $\beta_{EW} \approx 3.35$; the biases are lower for the other (lower) $\beta$, $H$ values. In the following, we therefore ignore this small effect.

[40] Figure 7 shows the $P$ contours obtained by taking averages over the squared moduli of the 2 × 365 transforms (0°–180°, 180°–0°; i.e., 2 per day for 2006): the spectra are shown with 2:1 aspect ratios such that circular large $k$ contours indicate isotropy. We note that this is more or less the case for the largest wave numbers corresponding to ~2 pixels (the Nyquist wave number) in real space. One sees that at larger and larger scales (smaller and smaller wave numbers, near the center), the contours become increasingly elliptical with the ellipses oriented in the $k_y$ direction corresponding to real-space structures extended in the east-west direction; overall the small Fourier space ellipses have aspect ratios ≈2. The only, but significant, exception is for the meridional wind which is also increasingly elliptical (by about the same amount) but elongated in the east-west rather than north-south direction. In comparison, for the fluxes there was also an EW elongation of structures but with the key difference that, due to the apparent isotropy of the flux exponents, their anisotropies were the same at all scales; i.e., there was "trivial anisotropy" of about the same factor (1.6 ± 0.3, section 3.1). In contrast, here the effect changes markedly with scale from near isotropy at single pixel scales to fairly strong stratification elongation at the largest scales. This scale by scale change of the aspect ratio combined with the scaling exhibited by the

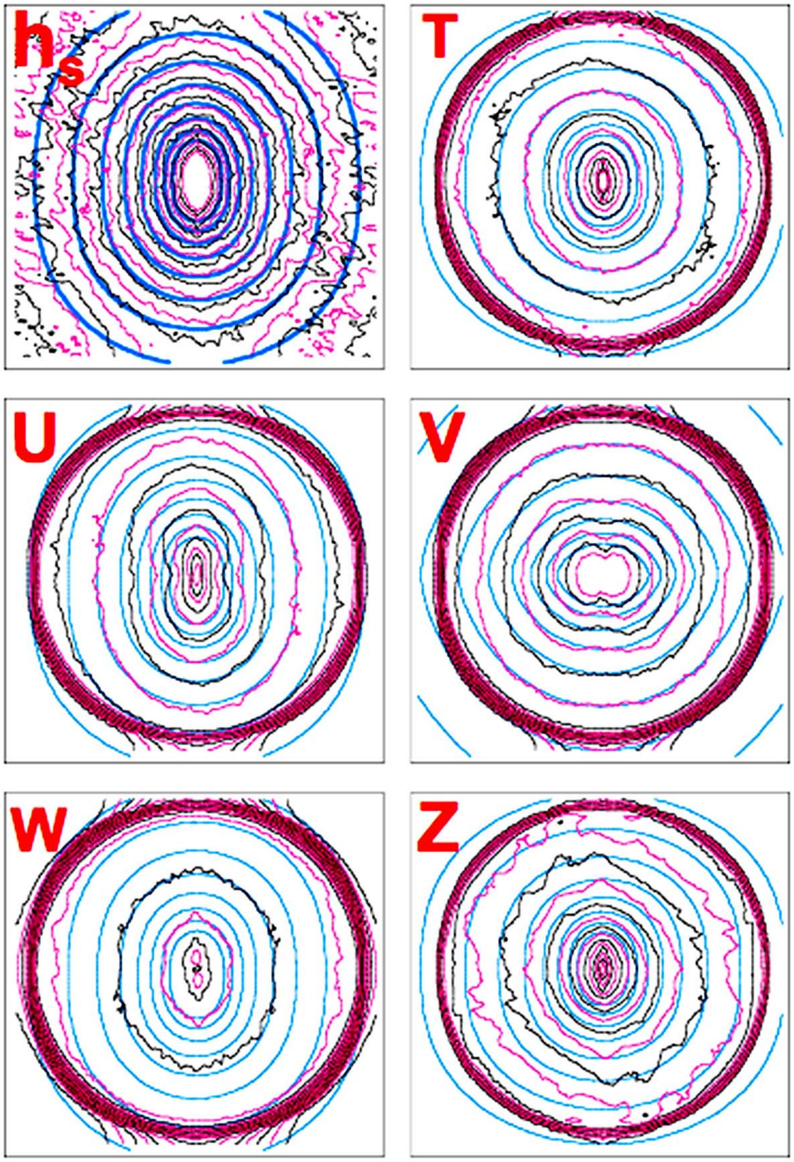

**Figure 7.** Contour plots of log $P$, left to right within plot is $k_x$, vertical direction is $k_y$. (top left) The specific humidity, (top right) temperature, (middle left) zonal and (middle right) meridional winds, (bottom left) vertical wind, and (bottom right) geopotential. Contours of the logarithm of the theoretical canonical scale functions (blue) all have $H_y = 0.8$ (except for $v$ which has $H_y = 1/0.8$) and the spherowave numbers are $k_s$ = 60, 30, 60, 30, 60, and 30 for $h_s$, $T$, $u$, $v$, $w$, and $z$, respectively. Due to the Nyquist frequency, the largest $k_y$ is 30 cycles/90° corresponding to 2 pixels. Due to the 2:1 aspect ratio (which compensates for the 2:1 change in range of $k_x$ with respect to $k_y$), a circle the diameter of the square in the image corresponds to isotropy at a 2 pixel scale.

fluxes suggests that the spectral density respects an anisotropic scaling symmetry:

$$P(\underline{k}) \propto \|\underline{k}\|^{-s} \tag{15}$$

where $\|\underline{k}\|$ is the (nondimensional) "scale function" which replaces the vector norm in scaling but anisotropic systems. $\|\underline{k}\|$ satisfies the functional scaling equation:

$$\|\lambda^{-G}\underline{k}\| = \lambda^{-1}\,\|\underline{k}\| \tag{16}$$

where $\lambda$ is a scale ratio and $G$ is the generator of the anisotropy; in the case where the anisotropy changes only with scale but not position, $G$ is a matrix ("linear generalized scale invariance," GSI). It is important to note that here we consider the scale by scale anisotropy of a scalar quantity; this is quite different from the more usual approach to anisotropy in the meteorological literature [e.g., *Hoskins et al.*, 1983] which considers the anisotropy of a vector quantity (e.g., the wind) at a unique (e.g., model resolution) scale.

[41] Here, in the horizontal ($x$, $y$) planar approximation to the Earth's surface, we take:

$$G = \begin{pmatrix} 1 & 0 \\ 0 & H_y \end{pmatrix} \tag{17}$$

and the simplest, "canonical" solution of the scale equation (16) with $G$ given by (17) is:

$$\|\underline{k}\| = \left( (k_x/k_s)^2 + (k_y/k_s)^{2/H_y} \right)^{1/2} \tag{18}$$

where $H_y$ is the ratio of the east-west and north-south scaling exponents and $k_s$ is the "spherowave number," the size of the roughly isotropic (circular) contours (equation (18) is a dimensionless scale function; a dimensional one can be obtained by multiplying by $k_s$). Note that the scale function equation (18) is only the simplest "canonical" scale function satisfying equations (16) and (17); for the more general case involving essentially an arbitrary "unit ball," see, e.g., *Lovejoy et al.* [2008]. What we are attempting here is to test equations (15), (16), and (17); this is a difficult problem in statistical parameter estimation; see, e.g., *Lewis et al.* [1999] for the "scale invariant generator technique" useful when $G$ is an arbitrary 2 × 2 matrix. Here we can use a more straightforward approach since $G$ is diagonal: to estimate the exponents we shall use both the zonal and meridional 1-D spectra, the 2-D isotropic spectrum and the 2D spectral density $P$.

[42] Before continuing, let us note that the real space counterpart to equations (15)–(18) is that the fluctuations in the field $\Delta f$ follow:

$$\Delta f(\underline{\Delta r}) = \varphi l_s^H \|\underline{\Delta r}\|^H; \qquad \underline{\Delta r} = (\Delta x, \Delta y);$$
$$\|\underline{\Delta r}\| = \left( (\Delta x/l_s)^2 + (\Delta y/l_s)^{2/H_y} \right)^{1/2} \tag{19}$$

where the real space "spheroscale" $l_s \approx 1/k_s$ and again, the canonical scale function in equation (19) is only the simplest; it need only satisfy the real space equation corresponding to equation (16). From equation (19) we see that the east-west ($\Delta x$) and north-south ($\Delta y$) exponents are different:

$$\Delta f(\Delta x, 0) \propto \Delta x^{H_{EW}}; \qquad \Delta f(0, \Delta y) \propto \Delta y^{H_{NS}};$$
$$H_{EW} = H; \qquad H_{NS} = H_{EW}/H_y \tag{20}$$

[43] One way to test equations (15) and (18) is to use the 1-D east-west and north-south spectra $E_{EW}(k_x)$ and $E_{NS}(k_y)$ obtained by integrating the $P$ defined by equations (15)–(18):

$$E_{EW}(k_x) = \int P(k_x, k_y) dk_y = A_x \left(\frac{k_x}{k_s}\right)^{-\beta_{EW}}; \qquad \beta_{EW} = s - H_y; \quad s > H_y$$
$$E_{NS}(k_y) = \int P(k_x, k_y) dk_x = A_y \left(\frac{k_y}{k_s}\right)^{-\beta_{NS}}; \qquad \beta_{NS} = \frac{s-1}{H_y}; \quad s > 1 \tag{21}$$

where $A_x$, $A_y$ are dimensionless constants of order unity (which will change somewhat depending on the exact scale function solution to equation (16); recall that the canonical scale function (equation (18)) is only a special case. A useful consequence of equation (21) is that it implies the following simple relation between exponents:

$$H_y = \frac{\beta_{EW} - 1}{\beta_{NS} - 1} \tag{22}$$

To determine space-space relations (between $k_x$, $k_y$) we can use the fact that the contribution to the total variance from all the structures smaller than a given wave number $k$ is given by the integral of $E(k')$ from $k$ to infinity. We can therefore exploit this fact to obtain a 1:1 relation (an implicit equation) between $k_x$ and $k_y$:

$$\int_{k_x}^{\infty} E_x(k_x') dk_x' = \int_{k_y}^{\infty} E_y(k_y') dk_y' \tag{23}$$

If $\beta_x > 1$, $\beta_y > 1$, then equation (23) (with the help of equations (21) and (22)) reduces to:

$$k_y = k_s' \left(\frac{k_x}{k_s'}\right)^{H_y} \tag{24}$$

where $k_s' \approx k_s$. (since $A_x \approx A_y \approx H_y \approx 1$). In other words, a simple way to check if the anisotropy is scaling is to directly determine the $k_x$, $k_y$ relation (equation (23)) from the 1-D spectra and then see if it is roughly a power law (equation (24)). For the key zonal and meridional winds, the corresponding space-space relations are shown in Figure 8. In Figure 8 we have used lines with slopes 1.25 (which closely fit the $u$ data) and slope 1/1.25 = 0.80 which closely fits the $v$ data (in both cases, the slopes = $1/H_y$). It is noteworthy that the scaling of the space-space relations in Figure 8 is superior to that of the individual zonal and meridional spectra (Figures 9b and 9c); this is possible because the latter have some residual deviations to scaling caused by the hyperviscosity. Our result is pleasingly symmetric since if we reflect the system about a northeast/southwest line, then $u$ and $v$ components as well as $x$ and $y$ axes are swapped and $H_y$ is replaced by $1/H_y$ so that this anisotropy respects this basic symmetry. Also shown in Figure 8 is the bisectrix; the point at which this line intersects the space-space $k_y(k_x)$ curve has $k_x = k_y = k_s'$, where $k_s'$ is the "spherowave number" (equation (24)). We see that $k_s'$ is indeed close to the largest wave number available (due to the Nyquist wave number, for $k_y$ this is 60/2 = 30 with $k_y = 1$ corresponding to $(10000 \text{ km})^{-1}$). Similarly, the maximum anisotropy is given by the extreme low $k_y$ aspect ratios, it corresponds to a factor $\approx 10^{0.3} \approx 2$.

[44] To test the idea further, we refer the reader to Figure 7 which shows the spectral densities $P$ with theoretical contours superposed corresponding to $H_y = 0.8$ (or for $v$, $H_y = 1/0.8 = 1.25$) and with $k_s$ fit to the nearest factor 2. It was found to be always either 30 or 60 cycles/10000 km corresponding to either twice the pixel scale of the public data (1.5°) or twice the pixel scale of the raw reanalysis data (0.7°).

### 4.1.3. The Implications of the Results

[45] In order to understand this anisotropic spectral behavior, let us note three key aspects of the results which appear to be robust: (1) the fields appear to have systematic scale by scale anisotropies whereas the corresponding

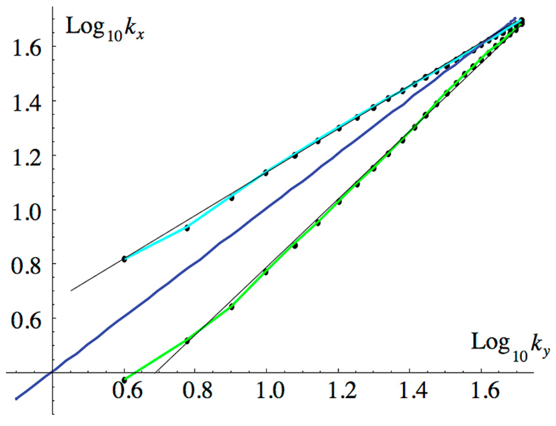

**Figure 8.** The empirical space-space relations for the zonal wind ($u$, green), and meridional wind ($v$, cyan) calculated using the implicit relation equation (23). The reference lines have slopes = $1/H_y$ = 0.8, 1, 1/0.8. The spherowave numbers are where the bisectrix (dark blue line) intersects the space-space lines.

turbulent fluxes do not, (2) the anisotropic exponent $H_y$ seems to be nearly the same for all fields (the only exception being $v$ for which it is the reciprocal as would be expected by symmetry), and (3) all the fields display an apparent isotropy at wave numbers corresponding to ~1.5° resolutions, i.e., very nearly the resolution of the reanalyses. Since, physically, there is nothing special at ~1.5° resolution that would make north-south and east-west fluctuations typically equal in magnitude (and this for all the fields), it would appear that the overall effect is an artifact of the numerics which have strong isotropic constraints at the (hyper) dissipation scale while at the same time having large scale anisotropies imposed by the boundary conditions. These large scale constraints correspond physically to the strong north-south gradients which are typically much larger than the east-west ones. This suggests that the models/reanalyses could be significantly improved by doubling their north south resolutions with respect to their east-west resolutions.

[46] We are making the perhaps surprising suggestion that boundary conditions could change scaling exponents. However, it is difficult to see how this could be otherwise since for the anisotropic scaling to have more profound causes, one would expect the fields to be dominated by physically different turbulent fluxes in the north-south and east-west directions, yet we have just shown (section 3) that the fluxes (which are responsible for the nonlinear contribution to the exponents $K(q)$, $\xi(q)$) seem only to display trivial anisotropy (i.e., $K_{EW}(q)/K_{NS}(q) = 1$ for the $\varphi$). It seems that the scaling anisotropy is restricted to the linear part ($\Delta x^H$ corresponds to a fractional integration of order $H$ of the turbulent flux $\varphi$, i.e., a linear operation), while the more fundamental nonlinear exponent $K(q)$ appears to be isotropic. The ability of the boundary conditions to introduce scaling anisotropy has in fact already been noted in radiative transfer on isotropic multifractal clouds when the boundary conditions are cyclic in the horizontal with radiative flux impinging from the cloud top only. The consequence is that the internal cloud radiative fluxes can have scaling anisotropies even when the cloud liquid water does not [*Lovejoy et al.*, 2009d].

[47] It is worth mentioning one last implication of the $H_y \approx 0.8$ differential horizontal scaling. If we consider the average area of horizontal structures as functions of their zonal extent, then we find $A \approx \Delta x \Delta x^{Hy} \approx \Delta x^{Del}$ where the effective "elliptical dimension" $D_{el} = 1 + H_y = 1.80$. This yields yet another argument against the relevance of two-dimensional isotropic turbulence to the atmosphere: even horizontal cross sections are not isotropic, they are not even two dimensional! If the atmospheric models (not just reanalyses) share this feature of having horizontal sections with $D_{el} = 1.80$, then it would seem that attempts such as those by *Takayashi et al.* [2006] to demonstrate the possible coexistence of 2D and 3D isotropic turbulent regimes are doomed to failure, if only because even the horizontal fails to display 2D isotropy.

## 4.2. The Isotropic Spectrum

[48] No matter what the correct explanation for the reanalysis horizontal anisotropy, it has consequences for estimates of the (supposedly) isotropic spectral exponents, and even for the extents of the scaling regimes. To see this, let us estimate the isotropic (angle integrated) spectrum (equation (13)) assuming that the spectral density $P$ has scaling anisotropy (i.e., that it has the form given by equations (15)–(18)); one then obtains:

$$\begin{aligned} E(k) &\approx k^{-\beta_l}; \qquad \beta_l = \min(\beta_{EW}, \beta_{NS}); \qquad k \ll k_s \\ E(k) &\approx k^{-\beta_h}; \qquad \beta_h = \max(\beta_{EW}, \beta_{NS}); \qquad k \gg k_s \end{aligned} \tag{25}$$

with $\beta_l$ the low, and $\beta_h$ the high wave number spectral exponents. We thus see that there is a break in the spectrum at $k_s$. Note that this break is spurious in the sense that it is a consequence of the isotropic integration; the full 2-D spectral density $P$ is perfectly scaling. However, $\beta_{EW}$ and $\beta_{NS}$ are related by equation (21) so that for $H_y < 1$:

$$\beta_l = \min(\beta_{EW}, \beta_{NS}) = \begin{matrix} \beta_{EW}; & \beta_{EW} > 1 \\ \beta_{NS}; & \beta_{EW} < 1 \end{matrix} \tag{26}$$

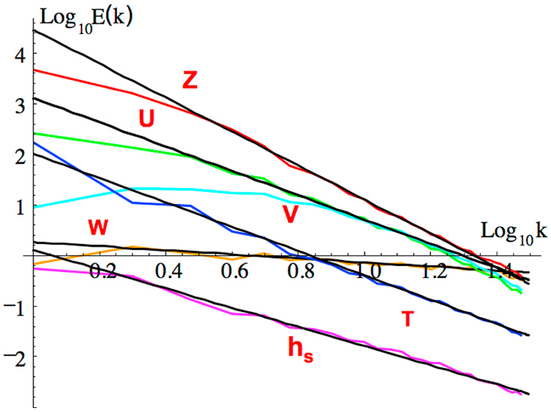

**Figure 9a.** The isotropic spectra estimated as discussed in the text by integrating $P$ over circular annuli. The reference lines have absolute slopes ($\beta$): 1.90, 2.40, 2.40, 2.40, 0.40, and 3.35 (for $h_s$, $T$, $u$, $v$, $w$, and $z$, respectively). The largest $k$ corresponds to an east-west distance of 20,000 km.

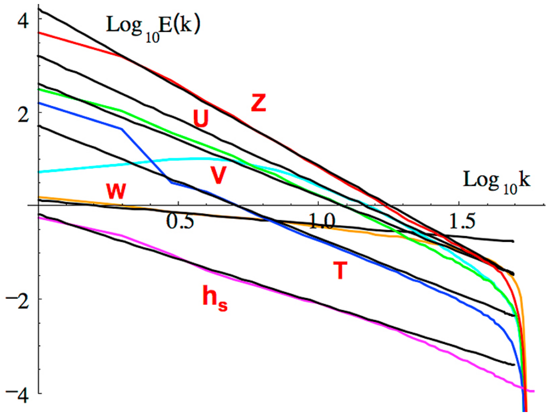

**Figure 9b.** The zonal spectra obtained by integrating $P$ in the $y$ (north-south) direction. The slopes of the reference lines are those predicted from the (more accurately estimated) isospectral slopes using equation (26). The reference lines have absolute slopes ($\beta$): 1.90, 2.40, 2.40, 2.75, 0.52, and 3.35 (for $h_s$, $T$, $u$, $v$, $w$, and $z$, respectively). The smallest wave number ($k$ = 1) corresponds to 20000 km.

with a corresponding equation for $\beta_h$ using the maximum rather than the minimum (and the converse inequalities for $H_y > 1$).

[49] Although the spectrum is not isotropic, if we are careful, we can still use the isotropic $E(k)$ which has the advantage of improving the estimates since the integration reduces the statistical fluctuations. Since we found that $k_s$ is very nearly the wave number corresponding to one pixel, we always have $k < k_s$ so that we do not expect a break; the isotropic exponent will always be $\beta_l$ (equations (25) and (26)). The approximation (equation (25)) improves at small $k$ so that good estimates can easily be obtained by estimating $P$ using numerical Fourier transforms over the available 120 × 60 point grids and then integrating the latter over circular annuli, keeping only the $k < 30$ part. Since there is a 2:1 aspect ratio, this is equivalent to integrating over ellipses with corresponding 2:1 aspect ratios; the same result (equation (25)) holds but the convergence to the power law $k^{-\beta_l}$ is faster.

[50] Figure 9a shows the results for the 6 fields; to make the scaling even more evident, we have averaged the spectrum over 10 logarithmically spaced intervals per order of magnitude (except for the lowest decade where all the wave numbers are indicated). Due to the 2:1 aspect ratio, the spatial scale corresponding to a wave number $k$ = 1 corresponds to 20000 km in the east-west and 10000 km in the north-south direction. From Figure 9a, we see that the scaling is generally excellent. The only exception is for the meridional wind which exhibits a sharp break at wave numbers corresponding to 1250–2500 km; for the low wave numbers it follows another scaling regime with $\beta \approx -0.2$ whose origin is obscure: it is far from any theoretically proposed value. Table 1 shows the values of the isotropic exponents $\beta_l$ estimated to the nearest 0.05.

[51] We can now use the relatively accurate isotropic exponent estimates to understand the 1-D spectra in the zonal and meridional directions (Figures 9b and 9c). Since the scaling is not as good as for the isotropic spectrum, we have added reference lines with the theoretical exponents (calculated from $\beta_l$ using formulae (25) and (26) above). We see that the agreement between the 1-D spectra and the lines theoretically predicted from the isotropic spectra is excellent.

[52] In order to understand the significance of the various $H$ exponents deduced from the spectra, recall that $H$ is the classical nonconservation parameter. In the fractionally integrated flux model [*Schertzer and Lovejoy*, 1987], it is also the order of fractional integration needed to obtain the field from a pure cascade ($H < 0$ corresponds to differentiation). Contrary to $\alpha$, $C_1$ which characterize the intermittent cascade processes and which can apparently only be evaluated numerically or empirically, $H$ is a value that traditionally has been estimated by dimensional analysis (e.g., the $H = 1/3$ in the Kolmogorov law). However, scanning the values in Table 1, several are problematic. Let us first consider the geopotential height $z$. Direct empirical estimates from the low wave number part of the (roughly) isobaric aircraft altitude spectrum from *Lovejoy et al.* [2009c] give $\beta \approx 4$ (but over a narrow range), i.e., a little larger than the ECMWF interim value ($\beta \approx 3.35$) in Table 1. This large value indicates that it varies very smoothly; the fact that it is greater than unity means that horizontal pressure derivatives are smooth: $\partial p/\partial x \approx \Delta p/\Delta x \approx \Delta x^{H-1}$ which for $H > 1$ is well behaved at small $\Delta x$. Turning our attention to $w$, although the $H$ was too difficult to reliably measure from aircraft, it was indirectly estimated from lidar backscatter from *Radkevitch et al.* [2008] as being in the range −0.1 to −0.2; this analysis is thus in agreement with small negative value (when H < 0, it implies that the fluctuations tend to cancel, that they diminish with scale; $H$ is then the exponent that determines the rate that the mean fluctuations are reduced by averaging).

[53] In order to understand the $H$ values for the wind, humidity and temperature, we have constructed Table 3. This compares the ECMWF reanalyses, aircraft [*Lovejoy et al.*, 2010] and dropsonde estimates [*Lovejoy et al.*, 2009b] (note, the meridional wind was not considered in the earlier studies). Starting with the wind, and concentrating on the zonal

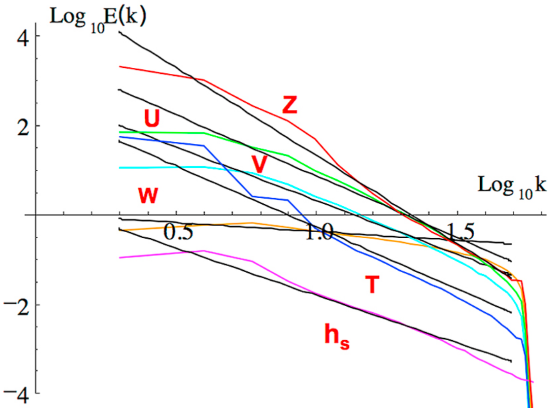

**Figure 9c.** The meridional spectra obtained by integrating $P$ in the $x$ (east-west) direction. The slopes of the reference lines are those predicted from the (more accurately estimated) isospectral slopes using equation (26). The reference lines have absolute slopes ($\beta$): 2.12, 2.75, 2.75, 2.40, 0.40, and 3.94 (for $h_s$, $T$, $u$, $v$, $w$, and $z$, respectively). The smallest wave number ($k$ = 1) corresponds to 20000 km.

**Table 3.** An Intercomparison of the ECMWF Interim Multifractal Parameters (Isobaric) With Those Estimated for Aircraft (Horizontal) and Drop Sondes (Vertical)[a]

| Source | $h$ | $T$ | $v$ |
|---|---|---|---|
| | | $\alpha_h$ | |
| ECMWF | 1.77 ± 0.06 | 1.90 ± 0.006 | 1.85 ± 0.012 |
| Aircraft | 1.81 | *1.78* | 1.94 |
| Drop sonde | 1.85 | 1.70 | 1.90 |
| | | $C_1$ | |
| ECMWF | 0.102 ± 0.009 | 0.077 ± 0.005 | 0.084 ± 0.006 |
| Aircraft | 0.083 | 0.108 | 0083 |
| Drop sonde | 0.072 | 0.091 | 0.088 |
| | | $H$ | |
| ECMWF | 0.54 | 0.77 | 0.77 |
| Aircraft | 0.51 ± 0.01 | 0.50 ± 0.01 | 1/3[b] |
| Drop sonde | 0.78 ± 0.07 | 1.07 ± 0.18 | 0.75 ± 0.05 |

[a] The aircraft $C_1$'s have been multiplied by the factor $(3/2)^{1.8} = 2.07$ in an attempt to take into account the fact that the aircraft measure scaling regime estimates of fluxes whereas the ECMWF estimates are more dissipation scale fluxes.

[b] Due to the issues of the vertical aircraft movement, this (Kolmogorov) value was inferred, not directly estimated [see *Lovejoy et al.*, 2010].

component we note that there is excellent agreement between the dropsonde (vertical) value and the ECMWF isobaric value. As argued by *Lovejoy et al.* [2009b], this is because the isobars are gently sloping so that at large enough scales, one obtains the vertical rather than horizontal values. As a consequence, the aircraft value given in Table 3 is the theoretical value 1/3 which was argued to be compatible with the small scale aircraft statistics when corrected for intermittent turbulent motions of the aircraft. The $H$ value for the humidity (0.54) is at least close to the measurements (0.51) although to our knowledge it is not predicted by any existing theory. Similarly the temperature $H$ is far from the aircraft $H$ although it is close to the isobaric wind $H$, suggesting that at least in the reanalysis, it is nearly hydrostatic: $T = gR^{-1}\partial z/\partial \ln p$ (it would then be an isobaric estimate rather than an isoheight estimate similar to the $H$ for the horizontal wind).

### 4.3. The Temporal Spectra

[54] To complete this overview of meteorological scale statistical exponents, we now turn to the time domain. From a theoretical point of view, the time domain is more complicated than the spatial domain, since even in classical isotropic turbulence, there exist two scaling exponents: one valid in Lagrangian frames (i.e., comoving with the flow) and one in the usual (fixed, Eulerian) frame. For the wind, the former yields $H = 1/2$ while the latter $H = 1/3$ (ignoring the small intermittency corrections, the corresponding spectral exponents are $\beta = 2$, 5/3, $K(2)$). These issues were discussed at length theoretically [*Lovejoy et al.*, 2008] and, for passive scalars, empirically by *Radkevitch et al.* [2008]. The upshot was that up to the scales of the weather/climate transition (~10 days) the Eulerian exponent would be expected to be dominant over the exponents arising from horizontal advection so that the classical $H = 1/2$ ($\beta \approx 2$) exponent would not be visible. However, if the vertical wind exponent has a slightly negative spatial $H$ (the values $\approx -0.1$ to $-0.2$ were quantitatively deduced, essentially the same as those found here; Table 1), then this, coupled with the nonclassical (anisotropic) scaling vertical stratification leads to a new complication: the possibility that the advection by the vertical velocity would yield an effective temporal exponent $H \approx 1/2$ ($\beta \approx 2$). This was indeed occasionally observed in the high-frequency passive scalar analyses and it has been occasionally reported in the literature for the wind (although the much more usual value is ~5/3 [see *Radkevitch et al.*, 2008]. However, the theory and analysis by *Radkevitch et al.* [2008] showed that this effect will only be visible for large vertical winds, small horizontal winds and at small space-time scales; hence for the ECMWF analyses we expect horizontal/temporal isotropy (i.e., the same exponents in space and time as found for the cascades).

[55] Figure 10a shows the temporal spectra over the entire observed frequency range (1 year)$^{-1}$ to the Nyquist frequency, (2 days)$^{-1}$. The overall shape of the spectrum is the same as that given by *Lovejoy and Schertzer* [1986]; i.e., starting at the high frequencies one has the scaling weather regime, then at lower frequencies one has the transition to the low-frequency weather regime (which starts to be visible at $\omega \approx$ (5 days)$^{-1}$ (i.e., at $\log_{10}(365/5) \approx 1.86$ in the graph), followed at still lower frequencies by a relatively flat "spectral plateau" climate regime (older spectra were presented in log linear plots of $\omega E(\omega)$ versus log $\omega$ [e.g., *Kolesnikov and Monin*, 1965] so that the transition appears as a maximum). This overall shape is the same as those reported by *Koscielny-Bunde et al.* [1998], *Pelletier and Turcotte* [1999] and *Talkner and Weber* [2000], *Huybers and Curry* [2006], and *Lennartz and Bunde* [2009] and is as predicted as a weather/low-frequency weather "dimensional transition" discussed above.

[56] Focusing on the high-frequency weather regime we see that it is narrow; Figure 10b shows a blow up of the

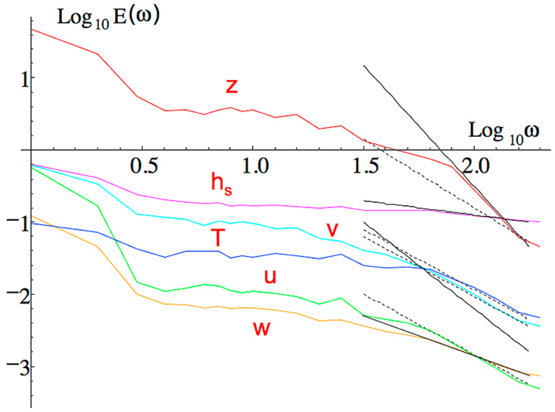

**Figure 10a.** The frequency spectrum with ensemble and spectral averaging (into 10 bins per order of magnitude for all $\omega > 36.5$ cycles/yr), units of $\omega$: cycles/yr. The dashed lines have slopes −5/3, and the solid lines have slopes −3.35, −0.4, −2.4, and −1.1 (top to bottom); they are drawn for $\omega >$ (11 days)$^{-1}$; for a blow-up of the high-frequency (weather) regime, see Figure 10b. These correspond to the spatial $z$ exponent, the spatial $w$ exponent (which accurately fits $h_s$), the spatial $u$, $v$, and $T$ exponent, and the regression $w$ slope, respectively. The curves from top to bottom (at left of plot) are $z$, $h_s$ (multiplied by 10 from the spatial analysis, i.e., the spectra are multiplied by 100), $v$, $T$, $u$, and $w$.

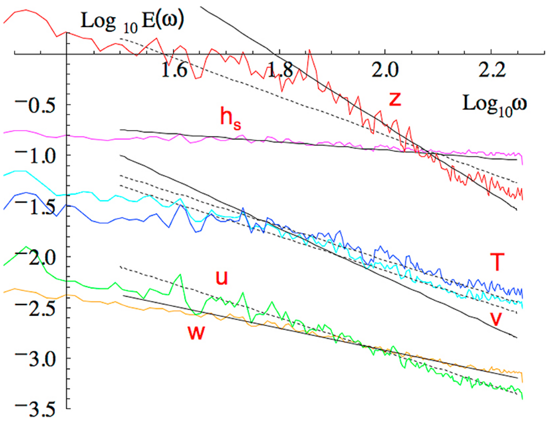

**Figure 10b.** Same as Figure 10a but a blow-up of the high-frequency decade ((20 days)$^{-1}$ to (2 days)$^{-1}$) using ensemble but not spectral averaging, units of $\omega$: cycles/yr. As in Figure 10a, the dashed lines have slopes −5/3, the solid lines have slopes −3.35, −0.4, −2.4, and −1.1 (top to bottom).

high-frequency decade. From this we see that regression estimates of the spectral exponent $\beta$ will depend somewhat on the regime used for the fit; it was therefore decided to use theoretically motivated reference lines rather than regressions, the only exception being the vertical velocity where a regression over $\omega > (5\ \text{days})^{-1}$ was used. The basic motivating theory was for the values 5/3 for $u$, $v$ and $T$ (as discussed for $u$, $v$ and as predicted if $T$ is a passive scalar), and the value 3.35 for $z$, which is obtained by using the isobaric value as an estimate of the horizontal exponent followed by space-time isotropy. The 5/3 values work very well for $u$, $v$, $T$ (the isobaric exponent 2.40 shown in Figure 10b is clearly very poor) but the isobaric value works well for $z$. In contrast, the exponents $\beta \approx 0.4$ ($h_s$) and $\beta \approx 1.10$ ($w$) have no clear theoretical explanation; although the value 0.4 for $h_s$ is very close to the isobaric $w$ value and could thus be a consequence of the fact that in the reanalysis, humidity fluctuations mostly arise from horizontal convergence which is highly correlated with the vertical wind which would then advect it in the vertical.

[57] In order to judge the realism of the temporal reanalysis exponents, we can compare them with in situ (surface) measurements (Table 4). In order to get the most accurate empirical estimates, where possible, literature values have been used (from high-frequency turbulence measurements); although for $z$, $h_s$ we were forced to use data from low resolution (daily) series originally analyzed for a climatological study (in this case, the surface pressure was used as a proxy for the geopotential height). As can be seen from Table 4, the $C_1$ and $\alpha$ values are reasonably close (although with some differences), and the $\beta$ and $H$ values are close enough to be considered "compatible" for the $u$, $v$, $T$, and $z$ fields (if we accept the surface pressure as a $z$ surrogate). For the vertical wind, there are no reliable in situ data of which we are aware ($w$ is extremely difficult to measure without statistical "contamination" from horizontal components). However, the isobaric and temporal exponents for $h_s$ are very different; but as mentioned above, the temporal $H$ exponent for $h_s$ is very close to the isobaric $w$ exponent. This suggests that the reanalyses do not adequately handle humidity. (Note that the statistics of relative and specific humidities were found to be extremely close so that the discrepancy cannot be attributed to this.)

## 4.4. Latitudinal Dependence of H and $\beta$

[58] We have already noted (section 3.3) that there was surprisingly little latitudinal variation in the cascade structure; we argued that this was likely to be a consequence of the fact that the cascade reflected the nonlinear interactions and that most of the latitudinal variations were due to the

**Table 4.** Temporal Scaling Exponents From the ECMWF Interim Reanalysis and From Various in Situ Estimates[a]

| Exponent | Source | $h_s$ | $T$ | $u$ | $v$ | $w$ | $z$ |
|---|---|---|---|---|---|---|---|
| $\beta$ | ECMWF | 0.40 | 5/3 | 5/3 | 5/3 | 1.10 | 3.35 |
| | In situ | 2.20[b] | 1.67 ± 0.04[c] | 1.68 ± 0.05[d,e] | 1.68 ± 0.05[d,e] | — | 3.00[f] |
| $C_1$ | ECMWF | 0.10 | 0.075 | 0.083 | 0.086 | 0.115 | 0.085 |
| | In situ | 0.09[b] | 0.087 ± 0.015[c] | 0.053 ± 0.010[d,e] | 0.053 ± 0.010[d,e] | — | 0.085[f] |
| $\alpha$ | ECMWF | 1.77 | 1.90 | 1.85 | 1.85 | 1.92 | 1.90 |
| | In situ | 1.8[b] | 1.61[c] | 1.5[d,e] | 1.5[d,e] | | 1.7[f] |
| H (time) | ECMWF | −0.21 | 1/3 | 1/3 | 1/3 | 0.17 | 1.26 |
| | In situ | 0.68[b] | 0.41 ± 0.03[c] | 0.33 ± 0.03[d,e] | 0.33 ± 0.03[d,e] | — | 1.07[f] |
| $H$ (space) | ECMWF (space) | 0.54 | 0.77 | 0.77 | 0.78 | −0.14 | 1.26 |
| | aircraft | 0.51 | 0.50 | 1/3[e] | 1/3[e] | — | — |

[a] The latter were taken from the literature and, when no other source was available, from daily station data that had been selected for a climate study; see the following footnotes for details. H time and space rows show the isobaric $H$ values estimated as discussed in the text; they are the zonal values (the only exception being the meridional wind where the meridional value is given). The $C_1$ and $\alpha$ estimates are from the flux analyses presented earlier, and the $H$ are estimated from the spectra (Figure 10). Due to the narrow range of frequencies (the Nyquist frequency (2 days)$^{-1}$ to about (5 days)$^{-1}$ before the spectra begins to flatten due to the transition to the low-frequency weather regime), direct estimates are not accurate and depend on the exact frequency range used. Instead, the spectral exponents were taken from the reference lines in Figure 10: for $T$, $u$, and $v$ they are seen to be compatible with the Kolmogorov value 5/3 (ignoring the intermittency corrections of $K(2)/2 \approx 0.08$), and for $h_s$ the value $\beta = 0.4$ is close to the data and is the same as the spatial $w$ value. Finally, the $\beta$ value for $z$ was close the spatial value (see Figure 10) and was used.

[b] Same study as in footnote f, but only 7 stations were near complete and longer than 60 years.

[c] The mean and standard deviations were calculated from the three published studies: *Finn et al.* [2001], *Schmitt et al.* [1996], and *Wang* [1995]; these are of high-frequency measurements near the surface.

[d] These numbers were calculated from *Schmitt et al.* [1994, 1996] and are from high-frequency (hot wire) data near the surface.

[e] No distinction was made between the zonal and meridional wind components; the same values were used for $u$ and $v$.

[f] These are estimates of surface pressure (not geopotential) statistics from 23 daily in situ series over (near complete) 60 years long in the continental United States (stations were taken every 2 degrees from 30° to 50° north and south, −105° to −71° east and west; only the longest, near complete series were used); the statistics are over the narrow range 2 days (Nyquist frequency) to 5 days (to avoid spectral flattening due to the weather/low-frequency weather transition).

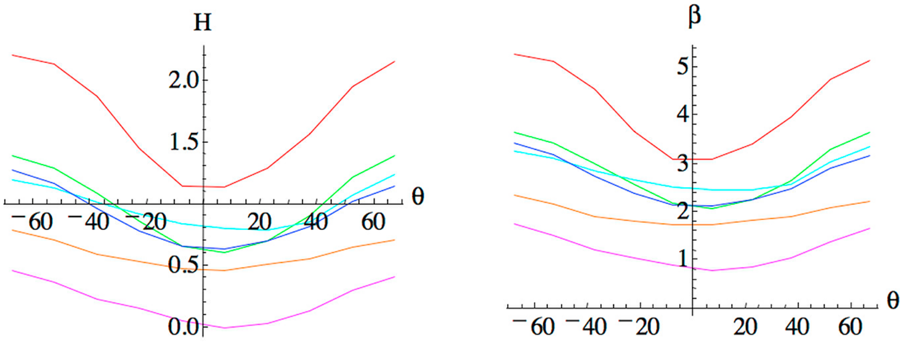

**Figure 11.** The (left) $H$ and (right) $\beta$ exponents estimated from zonal spectra from the 15° wide latitude bands discussed in section 3.3.

Coriolis force (a linear term) or to boundary conditions strongly varying in the north-south direction. It is therefore of interest to see how much the $H$ parameter (deduced from spectra or structure functions) varies with latitude. The main difficulties in spectral analyses are (1) that we have seen that the scaling range is not large due to hyperviscosity at small scales and to large scale spectral “roll-off” (flattening), and (2) the additional problem of strong north-south/east west anisotropy analyzed above. We therefore refer the reader to Figure 11 which gives the $\beta$ exponents (from zonal spectra over the admittedly narrow range $k = 6$ to 15) and the $H$ inferred from $\beta$, $C_1$, and $\alpha$. We see that the variation is quite symmetric between the two hemispheres, with the fields all being systematically rougher (lower $H$, $\beta$) near the equator. The reason for this is not clear, although the very large $\beta$ and $H$ values at the extremes away from the equator may be artifacts of the lower data density. The results are clearly less reliable than those discussed above and are probably not more accurate than ±0.1–±0.2 in $H$; this was the typical difference found when $H$ was estimated in real space using structure functions over the roughly the same scale range 600–2500 km). We do not give the corresponding temporal exponents since the scaling ranges are much too narrow (see the discussion above).

## 5. Conclusions

[59] Understanding the scale by scale statistical properties of reanalyses is important for several reasons. For one, they are frequently our only source of global scale information (e.g., the vertical wind field); in addition, their systematic scale by scale intercomparisons with the data are essential for developing more realistic reanalyses; finally, they are needed in ensemble forecasting systems since they specify the precise scale by scale statistical properties of the model. Previous studies have shown that the statistics follow nearly exactly the predictions of nonlinear theory: they have cascade structures to within about ±0.5% from 5000 km down to their inner (hyper) viscous scale in space, from about 5–10 days on down to 6 hourly or less in time. However, so far they have only provided a broad survey: they concentrated on the turbulent fluxes associated with the temperature, humidity, and zonal wind and considered the variation of statistical exponents (and outer scales) with altitude, latitude and forecast horizon, on intercomparisons between different products with atmospheric data.

[60] In this paper, we have focused on a single type of reanalysis—the ECMWF interim—and on a single pressure level (700 mbar), using the daily data for the year 2006 and we consider the observable fields themselves and their corresponding turbulent fluxes. Contrary to the fluxes, previous scaling analyses of the fields have generally not given clear results, and we here argue that the reason is the unexpected presence of scaling anisotropy in the horizontal fields (but not fluxes). In order to demonstrate this, we broke the data into Cartesian grids 180° × 90° (longitude × latitude, using a cylindrical projection from ±45° latitude) selecting a broader mix of fields for analysis: adding the meridional and vertical winds and the geopotential height to the previously studied zonal wind, temperature and humidity fields.

[61] The cascade flux analyses (in the zonal, meridional and temporal directions) gave nearly the same statistical exponents in each direction (“trivial anisotropy”) and (for $T$, $u$, and $h$) and the ECMFW interim products were close to those of the previously studied products (with similar exponents and similar external cascade scales: planetary in space and ~5 days in time). However, the spectra presented new and interesting problems connected with their horizontal anisotropies. Whereas the fluxes had aspect ratios of structures that were about 1.6:1 (zonal: meridional) but independent of scale, the fields showed distinct scaling anisotropies with aspect ratios increasing from 1 at single pixel scales to about 2:1 at the largest scales (again elongated in the zonal direction except for a predicted inversion for the meridional wind). While isotropy at a single pixel scale is likely to be an artifact of the reanalysis (hyper) viscosity, on the contrary the large scale anisotropy is physically based (a consequence of imposed strong north-south gradients). We therefore argued that this scaling anisotropy is likely to be a spurious consequence of the model being forced to join up a (spurious) isotropic small scale with a real (anisotropic) large scale and suggested that doubling the north-south resolution with respect to the east-west resolution might make an important improvement in the reanalyses. However, no matter what the cause of the anisotropy, if not carefully accounted for, it may lead to spurious breaks in the spectral scaling. The incautious use of isotropic data analysis techniques may therefore at least be partially responsible for the difficulty in establishing a consensus about the reanalysis spectra [see *Strauss and Ditlevsen* [1999].

[62] We also investigated the latitudinal dependence of the cascades and found that there was surprisingly little varia-

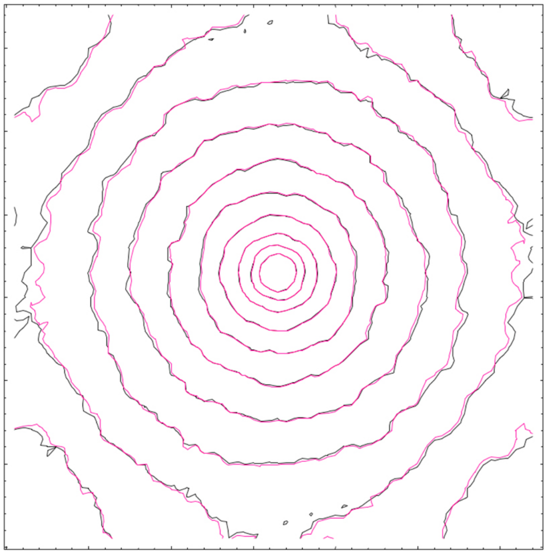

**Figure A1a.** The superposed contour plots of log$P$ (black) and log$P_p$ (red) for the simulations described in the text.

tion in the exponents, a consequence of the fact that the cascade structure reflects the nonlinear interactions whereas the main north-south variations are primarily due to Coriolis forces and boundary conditions. However, there were significant latitudinal variations of the prefactors, i.e., of the external space and time scales, and ratios (which are velocities relating space and time).

[63] Following careful treatment of the anisotropy, we found that the key new exponent $H$ (which can be interpreted as the degree of power law smoothing—fractional integration—needed to obtain the fields from their corresponding fluxes) has some interesting features. First, the $H$ exponents for $u$, $v$, and $T$ were systematically close to each other both in time, where they were close to the Kolmogorov value 1/3, and along isobars where they were close to the vertical exponent of the horizontal wind ~0.75. The similarity of the exponents makes it likely that in the reanalyses, the temperature is roughly hydrostatic; the nonstandard value 0.75 is probably an artifact of the gently sloping nature of the isobars which gives them a spurious vertical value [cf. *Lovejoy et al.*, 2009c]; the aircraft inferred isoheight values being the significantly lower ~0.50 ($T$) and ~1/3 ($u$, $v$). Turning our attention to the humidity, whereas along isobars it is close to the isoheight estimates from aircraft (~0.54 and 0.51, respectively), in time there is very large difference (~−0.21 and ~0.68 ECMWF isobars, in situ, respectively). Since the reanalysis humidity value (−0.21) is close to the reanalysis vertical wind value (−0.14), it may be a consequence the relation of both to the horizontal convergence. The vertical velocity also gave interesting results, with the ECMWF value (~−0.14) being roughly as predicted on the basis of lidar experiments, and the temporal value (~0.17) being quantitatively and qualitatively different (the sign). Unfortunately, we were unable to compare these to empirical estimates, although we should recall that the corresponding turbulent fluxes all gave results compatible with (horizontal) space-time scaling isotropy, and theoretical arguments also support that conclusion so that one should be somewhat suspicious of different horizontal spatial and temporal exponents. Similarly, the ECMWF geopotential height had nearly identical spatial and temporal values of $H$ (~1.26), but there was no good way to compare it with data; the closest was the surface pressure surrogate which gave a reasonably close value (~1.07), both indicating smooth isobaric surfaces (since $H > 1$).

[64] While this paper has extended the study of the scaling properties of reanalyses in several ways, there is still much to be done. A priority must surely be to better understand the vertical structure of the reanalyses: is the reanalysis capable of ingesting realistic scaling vertical/horizontal anisotropies; is the hydrostatic approximation a significant obstacle? Another outstanding question is the physical nature of the cascade quantities and the direction of the spectral transfers. Finally, we have indicated that the basic multiplicative model may still be valid at least some of the way into the low-frequency weather regime; indeed, work in progress shows that the low-frequency "spectral plateau" is indeed well modeled by simply extending the multifractal "fractionally integrated flux" model "calibrated" over meteorological space and time scales to much longer time scales (apparently up to decades [*Lovejoy and Schertzer*, 2011b, 2011c]). Durations of over 130 years are now possible with the 20th century reanalysis so that much lower frequency variability can be studied; such an understanding is necessary in order to formulate statistical tests which could distinguish natural from anthropogenic variability.

[65] Thanks to the ready availability of large quantities of global scale atmospheric data and the increasing maturity of nonlinear analyses and modeling techniques, Richardson's dream is in the process of being fully realized. This goes beyond the widely celebrated dream of numerical weather prediction to include his often forgotten contribution to the development of new emergent scaling turbulent laws. This new synthesis of nonlinear theory and state-of-the-art data sets and models relies on the exploitation of a nonclassical symmetry principle: scale invariance. For a long time, this symmetry was believed to be highly restrictive, applicable only to scale invariant systems which were also isotropic, hence the excessive focus of theorists with the paradigms of isotropic three dimensional and isotropic two dimensional turbulence. Unfortunately, these isotropic frameworks have largely prevented systematic, straightforward scaling statistical analyses of the atmosphere, and have contributed to today's unfortunate situation where there is still no consensus about the basic statistical properties of atmospheric fields as functions of space and time scales. Although the efforts to date are still only modest beginnings, they have convincingly shown that global scale satellite radiances, data from in situ aircraft, drop sondes, sparse surface networks, radars and lidars, and now reanalyses and other model products, are scaling over large ranges of space-time scales.

## Appendix A: The Effect of the Map Projection on the Spectra

[66] In statistically treating the ECMWF reanalysis and other spherical data sets gridded on equally spaced latitude and longitude grids, we remapped the ±45° latitude band using a cylindrical projection and performed standard analyses on these Cartesian grids. When performing 1-D

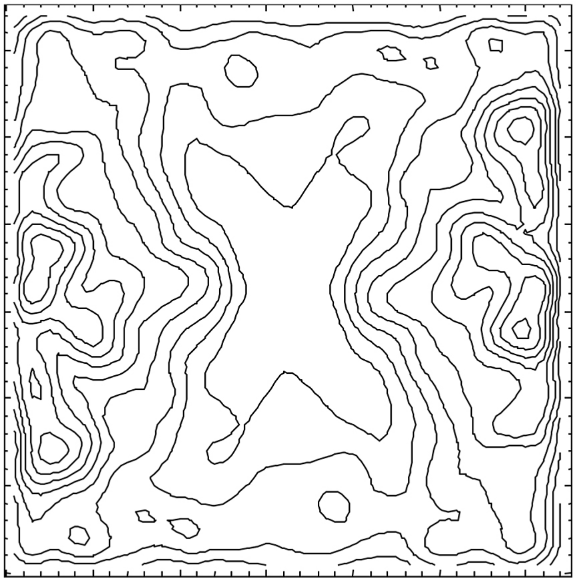

**Figure A1b.** The relative error field $E_r$ corresponding to Figure A1a. The maximum was 8.9%, and the mean was 3.6 ± 1.6%. The minimum (1.2%) is for the low wave numbers (the central contour), and the maximum is near the high wave numbers (edges).

analyses in either the zonal or meridional directions, it is sufficient to use a map factor which is only a function of latitude; this rescales the zonal results by the corresponding factor. However, since the map projection is itself anisotropic, the effects on the (Fourier, windowed) power spectral densities ($P(k_x, k_y)$) are less obvious and could potentially seriously contaminate our anisotropy analyses (section 4.1).

[67] In order to analyze this, we numerically simulated 365 isotropic multifractal fields with parameters $\alpha = 1.8$, $C_1 = 0.1$, $H = 0.333$ on 64 × 64 point grids (close to the year of zonal wind fields analyzed in section 4.1; this allows us to model the effects of the finite sample size as well). The resulting contour plots of log$P$ (original) and log$P_p$ (projection) are shown in Figure A1a. It can be seen that they are so close so that it is very hard to distinguish them; there is virtually no sign of any anisotropy. Figure A1b quantifies this; it shows contours of the relative difference between the two spectral densities:

$$E_r = 2\frac{|P - P_p|}{P + P_p} \tag{A1}$$

[68] On a pixel by pixel basis, we find $E_r = 3.6 \pm 1.6\%$ (the maximum value was 8.9%), i.e., a very small bias with an even smaller deviation around the mean; the central (low wave number) region of Figure A1b has deviations <2%, and the higher deviations are at the larger wave numbers. This should be compared with the actual variation of the density $P$ which varies over 4 orders of magnitude. Notice that this numerical result also takes into account the effect of the north-south discontinuity introduced by the map projection (which is handled with a standard Hann window), whereas the original field was periodic by construction and had no such edge effects.

[69] The effect of the map anisotropy increases with $H$; we therefore also considered its effect on the geopotential which had the largest $H$ (= 1.26; see Table 4). We now find that the mean deviation ($E_r$, equation (A1)) is ±5% for a 2-D spectral density which for $\beta = 3.3$ varies over more than 5 orders of magnitude (this is for the full range of wave numbers with the exception of the largest factor of 2 which for the reanalyses are artificially smooth due to their hyperviscosities). However, the main point is to find out whether the spectrum has systematically different exponents in the meridional and zonal directions and if so whether or not this might be a mapping artifact. We therefore compared the exponents of the 1-D spectra in east-west and north-south directions. Still for the $H = 1.25$ case, for the original (unmapped) spectra the exponents differ by 0.005 whereas for the mapped, they differ by 0.01 and 0.05 (zonal and meridional, respectively), so that there is indeed a small but detectable mapping anisotropy. However, this should be compared to the actual ECMWF exponents of 3.35 (zonal) and 3.94 (meridional) so that the actual difference in the exponents is ~0.5; i.e., it is ten times larger than any bias introduced by the mapping. Again the anisotropy introduced by the mapping is a very small effect.

[70] The reason that the map projection gives such a small effect is that (1) it only strongly effects a relatively small number of pixels while (2) it simultaneously affects all scales (at a given latitude) by a constant factor (ranging between 1 (equator) and $2^{1/2} = 0.707$ (at ±45°)) and (3) the spectrum thus throws away the phase effectively averaging over all the pixels. The much stronger effect shown in Figure 7 is a scale by scale statistical anisotropy effect.

[71] In any case, we should recall that the ECMWF exponents were not estimated simply from nonlinear regressions since for each field we needed two exponents s and $H_z$ which were constrained by the full 2-D density $P$ (Figure 7), the three spectra Figures 9a, 9b, and 9c (isotropic, zonal and meridional), as well as the physical constraint that there be a single $H_z$ value for all the six fields.

[72] **Acknowledgments.** We thank G. Compo, P. Sardeshmuhk, and C. Penland for useful discussions and the NOAA Climate Diagnostic Center and the Cooperative Institute for Research in Environmental Sciences (CIRES) for hosting me and supporting this research during my 2009–2010 sabbatical leave.

## References

Berrisford, P., et al. (2009), The ERA Interim Archive, *ERA Rep. Ser. 1*, ECMWF, Reading, U. K.

Boer, G. J., and T. G. Shepherd (1983), Large scale two-dimensional turbulence in the atmosphere, *J. Atmos. Sci.*, *40*, 164–184, doi:10.1175/1520-0469(1983)040<0164:LSTDTI>2.0.CO;2.

Bolgiano, R. (1959), Turbulent spectra in a stably stratified atmosphere, *J. Geophys. Res.*, *64*, 2226–2229, doi:10.1029/JZ064i012p02226.

Compo, G. P., et al. (2011), The Twentieth Century Reanalysis Project, *Q. J. R. Meteorol. Soc.*, *137*, 1–28, doi:10.1002/qj.776.

Finn, D., et al. (2001), Multifractal analysis of plume concentration fluctuations in surface layer flows, *J. Appl. Meteorol.*, *40*, 229–245, doi:10.1175/1520-0450(2001)040<0229:MAOLSP>2.0.CO;2.

Gires, A., I. Tchiguirinskaia, D. Schertzer, and S. Lovejoy (2011), Analyses multifractales et spatio-temporelles des précipitations du modèle Méso-NH et des données radar, *Hydrol. Sci. J.*, *56*(3), 380–396, doi:10.1080/02626667.2011.564174.

Hoskins, B. J., et al. (1983), The shape, propagation and mean-flow interaction of large-scale weather systems, *J. Atmos. Sci.*, *40*, 1595–1612, doi:10.1175/1520-0469(1983)040<1595:TSPAMF>2.0.CO;2.

Huybers, P., and W. Curry (2006), Links between annual, Milankovitch, and continuum temperature variability, *Nature*, *441*, 329–332, doi:10.1038/nature04745.

Kolesnikov, V. N., and A. S. Monin (1965), Spectra of meteorological field fluctuations, *Izv. Russ. Acad. Sci. Atmos. Oceanic Phys., Engl. Transl.*, *1*, 653–669.

Kolmogorov, A. N. (1941), Local structure of turbulence in an incompressible liquid for very large Reynolds numbers, *Izv. Akad. Nauk. SSSR Ser. Geofiz.*, *30*, 299–303.

Koscielny-Bunde, E., et al. (1998), Indication of a universal persistence law governing atmospheric variability, *Phys. Rev. Lett.*, *81*, 729–732, doi:10.1103/PhysRevLett.81.729.

Lennartz, S., and A. Bunde (2009), Trend evaluation in records with long term memory: Application to global warming, *Geophys. Res. Lett.*, *36*, L16706, doi:10.1029/2009GL039516.

Lewis, G., et al. (1999), The scale invariant generator technique for parameter estimates in generalized scale invariance, *Comput. Geosci.*, *25*, 963–978, doi:10.1016/S0098-3004(99)00061-8.

Lindborg, E. (1999), Can the atmospheric kinetic energy spectrum be explained by two-dimensional turbulence?, *J. Fluid Mech.*, *388*, 259–288, doi:10.1017/S0022112099004851.

Lindborg, E., and J. Cho (2001), Horizontal velocity structure functions in the upper troposphere and lower stratosphere: 2. Theoretical considerations, *J. Geophys. Res.*, *106*, 10,233–10,241, doi:10.1029/2000JD900815.

Lovejoy, S., and D. Schertzer (1986), Scale invariance in climatological temperatures and the spectral plateau, *Ann. Geophys., Ser. B*, *4*, 401–410.

Lovejoy, S., and D. Schertzer (2010), Towards a new synthesis for atmospheric dynamics: Space-time cascades, *Atmos. Res.*, *96*, 1–52, doi:10.1016/j.atmosres.2010.01.004.

Lovejoy, S., and D. Schertzer (2011a), *The Emergence of Atmospheric Dynamics: Multifractal Cascades*, 400 pp., Cambridge Univ. Press, Cambridge, U. K.

Lovejoy, S., and D. Schertzer (2011b), The emergence of the climate. Part I: An empirical overview, in *Complexity and Extreme Events in Geosciences*, *Geophys. Monogr. Ser.*, edited by A. S. Sharma et al., in press.

Lovejoy, S., and D. Schertzer (2011c), The emergence of the climate. Part II: Theory, in *Complexity and Extreme Events in Geosciences*, *Geophys. Monogr. Ser.*, edited by A. S. Sharma et al., in press.

Lovejoy, S., et al. (1986), Fractal characterisation of inhomogeneous measuring networks, *Nature*, *319*, 43–44, doi:10.1038/319043a0.

Lovejoy, S., et al. (2004), Fractal aircraft trajectories and nonclassical turbulent exponents, *Phys. Rev. E*, *70*, 036306, doi:10.1103/PhysRevE.70.036306.

Lovejoy, S., et al. (2008), Scaling turbulent atmospheric stratification, Part I: Turbulence and waves, *Q. J. R. Meteorol. Soc.*, *134*, 277–300, doi:10.1002/qj.201.

Lovejoy, S., D. Schertzer, V. Allaire, T. Bourgeois, S. King, J. Pinel, and J. Stolle (2009a), Atmospheric complexity or scale by scale simplicity?, *Geophys. Res. Lett.*, *36*, L01801, doi:10.1029/2008GL035863.

Lovejoy, S., A. F. Tuck, S. J. Hovde, and D. Schertzer (2009b), The vertical cascade structure of the atmosphere and multifractal drop sonde outages, *J. Geophys. Res.*, *114*, D07111, doi:10.1029/2008JD010651.

Lovejoy, S., et al. (2009c), Reinterpreting aircraft measurements in anisotropic scaling turbulence, *Atmos. Chem. Phys.*, *9*, 5007–5025, doi:10.5194/acp-9-5007-2009.

Lovejoy, S., et al. (2009d), Scattering in thick multifractal clouds, Part II: Multiple scattering, *Physica A*, *388*, 3711–3727.

Lovejoy, S., A. F. Tuck, and D. Schertzer (2010), The horizontal cascade structure of atmospheric fields determined from aircraft data, *J. Geophys. Res.*, *115*, D13105, doi:10.1029/2009JD013353.

Lucarini, V., and F. Ragone (2011), Energetics of climate models: Net energy balance and meridional enthalpy transport, *Rev. Geophys.*, *49*, RG1001, doi:10.1029/2009RG000323.

Obukhov, A. (1959), Effect of Archimedean forces on the structure of the temperature field in a turbulent flow, *Dokl. Akad. Nauk SSSR*, *125*, 1246–1249.

Pelletier, J. D., and D. Turcotte (1999), Self-Affine Time series II. Applications and models, *Adv. Geophys.*, *40*, 91–166, doi:10.1016/S0065-2687(08)60294-0.

Radkevitch, A., et al. (2008), Scaling turbulent atmospheric stratification, Part III: Empirical study of space-time stratification of passive scalars using lidar data, *Q. J. R. Meteorol. Soc.*, *134*, 316–335, doi:10.1002/qj.1203.

Schertzer, D., and S. Lovejoy (1984), On the dimension of atmospheric motions, in *Turbulence and Chaotic Phenomena in Fluids*, edited by T. Tatsumi, pp. 505–512, Elsevier Sci., Amsterdam.

Schertzer, D., and S. Lovejoy (1985a), Generalised scale invariance in turbulent phenomena, *Phys. Chem. Hydrodyn. J.*, *6*, 623–635.

Schertzer, D., and S. Lovejoy (1985b), The dimension and intermittency of atmospheric dynamics, in *Turbulent Shear Flow 4*, edited by B. Launder, pp. 7–33, Springer, New York.

Schertzer, D., and S. Lovejoy (1987), Physical modeling and analysis of rain and clouds by anisotropic scaling of multiplicative processes, *J. Geophys. Res.*, *92*, 9693–9714, doi:10.1029/JD092iD08p09693.

Schertzer, D., and S. Lovejoy (1992), Hard and soft multifractal processes, *Physica A*, *185*, 187–194, doi:10.1016/0378-4371(92)90455-Y.

Schertzer, D., and S. Lovejoy (1997), Universal multifractals do exist!, *J. Appl. Meteorol.*, *36*, 1296–1303, doi:10.1175/1520-0450(1997)036<1296:UMDECO>2.0.CO;2.

Schertzer, D., et al. (1997), Multifractal cascade dynamics and turbulent intermittency, *Fractals*, *5*(3), 427–471, doi:10.1142/S0218348X97000371.

Schmitt, F., et al. (1994), Estimation of universal multifractal indices for atmospheric turbulent velocity fields, *Fractals*, *3*, 568–575.

Schmitt, F., et al. (1996), Universal multifractal structure of atmospheric temperature and velocity fields, *Europhys. Lett.*, *34*, 195–200, doi:10.1209/epl/i1996-00438-4.

Stolle, J., et al. (2009), The stochastic cascade structure of deterministic numerical models of the atmosphere, *Nonlinear Process. Geophys.*, *16*, 607–621, doi:10.5194/npg-16-607-2009.

Strauss, D. M., and P. Ditlevsen (1999), Two-dimensional turbulence properties of the ECMWF reanalyses, *Tellus, Ser. A*, *51*, 749–772.

Takayashi, Y. O., et al. (2006), Explicit global simulation of the meso-scale spectrum of atmospheric motions, *Geophys. Res. Lett.*, *33*, L12812, doi:10.1029/2006GL026429.

Talkner, P., and R. O. Weber (2000), Power spectrum and detrended fluctuation analysis: Application to daily temperatures, *Phys. Rev. E*, *62*, 150–160, doi:10.1103/PhysRevE.62.150.

Wang, Y. (1995), Measurements and multifractal analysis of turbulent temperature and velocity near the ground, MSc. thesis, McGill Univ., Montreal, Quebec, Canada.

---

S. Lovejoy, Department of Physics, McGill University, 3600 University St., Montreal, QC H3A 2T8, Canada. (lovejoy@physics.mcgill.ca)

D. Schertzer, Laboratoire Eau Environnement Systèmes Urbains, Ecole des Ponts ParisTech, Université Paris Est, 6-8 Av. B. Pascal, F-77455 Marne-la-Vallée CEDEX 2, France.